DEVELOPMENT OF MEMS POWER INDUCTORS WITH SUBMICRON LAMINATIONS USING AN AUTOMATED ELECTROPLATING SYSTEM

A Thesis
Presented to
The Academic Faculty

by

Urvi Shah

In Partial Fulfillment
of the Requirements for the Degree
Master of Science in the school of Electrical and Computer Engineering,
GEORGIA INSTITUTE OF TECHNOLOGY

Georgia Institute of Technology
December 2007

DEVELOPMENT OF MEMS POWER INDUCTORS WITH SUBMICRON LAMINATIONS USING AN AUTOMATED ELECTROPLATING SYSTEM

Approved by:

Dr. Mark G. Allen, Advisor
School of Electrical & Computer Engineering
Georgia Institute of Technology

Dr. Deepakraj M. Divan
School of Electrical & Computer Engineering
Georgia Institute of Technology

Dr. David G. Taylor
School of Electrical & Computer Engineering
Georgia Institute of Technology

Date Approved: November 13, 2007

Dedicated

To my parents Mr. Parag Shah and Mrs. Avani Shah

ACKNOWLEDGEMENTS

I would like to take this opportunity to thank all the people who supported and inspired me during my research. I am greatly indebted to my advisor, Dr. Mark Allen for his guidance and patience throughout my pursuit of the MS degree. I would like to thank him for giving me this wonderful opportunity to work in his research group. I would like to express my sincere gratitude to Dr. David Taylor and Dr. Deepakraj Divan for serving on my thesis committee and providing invaluable support.

A warm thank you to all the members of Micro Sensors and Micro Actuators group for their friendship, help and advice. Many thanks to the members of the 'Magnetics' subgroup, especially Dr. Seong-Hyok Kim and Preston Galle for their valuable insights and help in the fabrication process. I would also like to thank Richard Shafer for his help in obtaining materials and constructing the robot. A special thank you to Seong-O Choi and Nisarga Naik for their help in conducting last-minute experiments!

Finally, I would like to thank my family and friends whose faith has been my driving force. I would not have been able to achieve this important milestone without them.

TABLE OF CONTENTS

LIST OF TABLES

LIST OF FIGURES

SUMMARY

The objective of the proposed research is to use MEMS technology to develop low profile power inductors with minimized eddy current losses to be used in high power density compact switching converters. Eddy currents arise in high-flux density metallic cores as increased switching frequencies of DC-DC converters cause the skin depth to be small compared with the core thickness. Laminations can reduce the eddy current losses but converters operating with switching frequencies in the MHz regime may require submicron laminations. Previous research has been done to fabricate inductors with micron-scale laminated cores for high frequency switching converters. To optimize the previous fabrication technique, an automated electroplating system was developed for the fabrication of thick magnetic cores comprising large number of submicron laminations without human intervention. Inductors with higher inductance, quality factor and power handling capacity have been realized compared to previously developed inductors. The inductors are characterized in terms of saturation behavior and power handling capability. A miniaturized DC-DC converter with power conversion capacity of 10 Watts has been demonstrated using the fabricated inductor.

CHAPTER 1: INTRODUCTION

The last few decades in electronics, especially for portable and telecom applications can be described in one word- miniaturization. There is a growing demand for higher power density and better power conversion efficiency for power supply devices installed in portable electronic equipment such as cell phones and PDAs. This has led to (1) switch-mode regulators gaining popularity over conventional linear regulators; and (2) optimization of passive components, especially magnetic, as they are the bulkiest elements in these modules. Structural integration of these magnetic components can prove to be a good solution to increase the power density. The magnetic material used plays a crucial role in the design of any magnetic component.

1.1 Power Inductors

1.1.1 Inductor Basics

An inductor is a passive circuit element formed by the linkage of magnetic flux and current, typically formed by winding a coil around a core. The core may comprise either air, a non-magnetic or magnetic material. The current in the coil induces a magnetic field that changes with change in direction of the current. The changing magnetic field induces an electromotive force to oppose the change in current. The characteristic of the inductor to resist the change in current makes it very useful in power converters. The inductance of an inductor is given by:

$$L = \frac{\lambda}{i} \tag{1.1}$$

where λ is the flux linkage and *i* is the time varying current.

A practical inductor can be modeled as shown in figure 1.1(a). The impedance Z of the inductor can be represented as the sum of a real part, representing the DC and AC resistance of the windings and the resistance associated with the core losses (hysteresis and eddy current losses); and an imaginary part, incorporating not only the inductance but also a distributed capacitance comprising the turn-to-turn and winding-to-core capacitances. Figure 1.1(b) shows the frequency response of the inductor. The inductor becomes purely resistive at the resonance frequency when the parasitic capacitance and the inductance resonate. The inductor has an inductive reactance below that frequency and behaves like a capacitor above that frequency. The quality factor of an inductor is the ratio of its inductive reactance to its resistance at a given frequency.

$$Q = \frac{\omega L}{R} \tag{1.2}$$

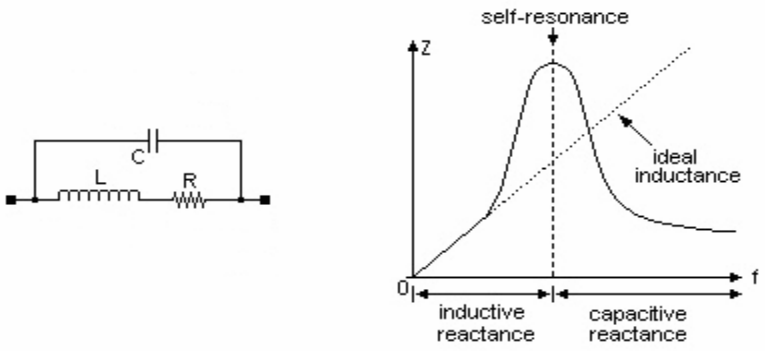

(a) (b)

Figure 1.1 Frequency response of a non-ideal inductor [1]

The quality factor shows the amount of energy stored versus the power loss incurred. If R is negligible, the Q factor is infinite and the inductor is ideal and lossless. A subset within the broad inductor category, the power inductor is used in switch mode power supplies as an energy storage element and a current ripple filter. The magnetic

energy stored by an inductor, can be expressed as

$$W_H = \frac{1}{2}\int_{vol} \vec{B} \bullet \vec{H} dv = \frac{1}{2}\int_{vol} \frac{\vec{B}^2}{\mu} dv \tag{1.3}$$

where $\vec{B}$ is the magnetic flux density vector, $\vec{H}$ is the magnetic field intensity and μ is the permeability of the core. The core material is assumed to be linear and homogenous.

The maximum energy stored in the inductor for uniformly distributed magnetic field in the core is given by:

$$W_{\max} = \frac{B_{sat}{}^2 V_{core}}{2\mu} \tag{1.4}$$

where V_{core} is the volume of the core, μ is the permeability, B_{sat} is the saturation flux density.

For smaller real estate consumption, thickness of the core decides the energy storage capacity of the device. The maximum power handling capacity is the energy stored over one switching time period.

$$P_{\max} = \frac{B_{sat}{}^2 V_{core}}{2\mu T_{SW}} = \frac{B_{sat}{}^2 V_{core} f_{SW}}{2\mu} \tag{1.5}$$

where f_{SW} is the switching frequency of the converter.

1.1.2 Core Material

Inductors and transformers used in portable power management applications require soft magnetic films with low coercivity, high permeability and large ferromagnetic resonance frequencies. Due to their high permeability, ferromagnetic

materials such as crystalline metal alloys, amorphous metal alloys and ferrites are commonly used as core materials. The core material should be chosen such that it provides high resistivity to reduce eddy current loss at high frequency, low hysteresis loss for high efficiency, fairly simple fabrication process and capability of integrated fabrication with ICs. Eddy currents are circulating currents induced in the core by the alternating magnetizing field. The induced eddy currents produce a magnetic field counteracting the magnetizing field to reduce the net magnetic flux in the core and at higher frequencies, shield it from the inner portion of the core cross-section. This phenomenon is called the magnetic skin effect. The decay of magnetic flux from the surface to the inner portion is exponential in nature and the core depth at which the flux decays to 1/e of the surface value is the skin depth given by equation 1.6. The skin depth decreases and the skin effect becomes more significant with increase in the conductivity σ, angular frequency ω and permeability μ.

$$\delta = \sqrt{\frac{2}{\omega \mu \sigma}} \tag{1.6}$$

Use of high resistivity materials (thereby making the skin depth large) or cores with laminations of considerably small thickness compared to the skin depth at the frequency of interest, greatly reduces the eddy currents and the losses associated with them.

Ferrite cores have relatively high resistivity and hence low eddy current losses and are predominant in the market for switching operation in the range of 1MHz to 10MHz [2]. The major drawbacks of ferrite cores are the low saturation flux density (0.3 to 0.5T) and lack of robustness, limiting their use in high power applications. Metal

alloys such as Nickel Iron and Cobalt Iron have a much higher saturation flux density (0.8 to 2.4 T) and a higher Curie temperature compared to ferrite cores, making them ideal candidates for high power density devices [3]. But, metal alloys suffer from low resistivity. In ferrite cores, eddy current losses overtake hysteresis loss at 200-300 kHz while in metal alloy cores, eddy current losses dominate above a few hundred Hertz. Sputtered metallic films with resistivity higher than 100μΩ-cm have been reported [4] but it is difficult to get sufficient thickness of sputtered films for high power applications. To overcome the limitations in sputtered and electroplated laminations, highly laminated low profile magnetic cores with micron scale laminations and high power handling (≥ 1W) have been demonstrated using high permeability metallic alloys [5]. The fabrication process has been described in Chapter 2. The laminations are very thin compared to the skin depth in the lower MHz regime and the core has very low eddy current losses as the resistance of each lamination is very high compared to a bulk core.

1.2 Research Objectives

In [6], the fabrication technique involves electroplating of alternate layers of magnetic laminations and non-magnetic sacrificial material. As the frequency of operation increases, the lamination thickness must be decreased and for the same core thickness, a larger number of laminations is required. It is not practical to manually electroplate >10 layers because of the time and effort involved to obtain several laminations of precise thickness. The goal of this research is to optimize the fabrication process in [6] to develop low profile inductors with high power handling (≥ 10 W) by:

1) Development of an automation system to carry out controlled electroplating of

alternate metal layers without human intervention;

2) Development of thick magnetic cores having large number of submicron laminations using the automation system;

3) Demonstration of a high power DC-DC switching converter using the fabricated inductors.

CHAPTER 2: MEMS BASED CORE LAMINATION TECHNIQUE USING SACRIFICIAL ETCHING

Previous work has been done to reduce eddy currents by fabricating inductors with mechanical laminations made by hot press [7] and horizontal laminations using electroplating and sequential sputtering [8], [9]. The fabrication process used in [6] involves core fabrication by sequential electroplating followed by sacrificial layer etching to achieve micron level laminations that cannot be attained using mechanical laminations and the process does not require interposing vacuum steps involved in horizontal sputtering. In this research, the fabrication process described in [6] has been modified to allow fabrication of thicker magnetic cores. $Nickel_{80}$ $Iron_{20}$ is selected as the core material because of its high permeability and saturation flux density. Table 2.1 shows the composition of the NiFe plating solution. The pH of the plating solution is maintained between 2.5 and 3.3 at room temperature. The plating rate of NiFe is 0.15μm/min for a plating current of 250mA. Copper is selected as the non-magnetic sacrificial material. Copper shows a very good etching selectivity over Nickel Iron in saturated cupric sulfate - ammonium hydroxide etch. Other possible combinations of electrodeposited metals with high etching selectivity over each other are CoFe and Copper. Nickel Iron alloys of varying composition have different etch rates and the etching of the more iron rich alloys with no effect on the nickel rich structures has led to in situ formation of sacrificial layers in electrodeposited NiFe to form planar thin films and microgears [10].

Table 2.1 Composition of NiFe electroplating solution [11]

Ingredients	**Quantity**
$NiSO_4$-$7H_20$	200 (g/l)
$FeSO_4$-$7H_2O$	8 (g/l)
$NiCl_2$-$6H_20$	5 (g/l)
H_3BO_3	25 (g/l)
Saccharin	3 (g/l)

2.1 Fabrication Process

A seed layer (Ti-Cu-Ti) is deposited on an oxidized silicon substrate. A coat of thick photo resist (NR2-25000) is applied and patterned to form a mold having two high aspect ratio windows of thickness 180 μm separated by a 200 μm wide wall. Alternate layers of $Nickel_{80}$-$Iron_{20}$ and copper are sequentially plated through the mold, each layer providing a good electrical base for the electrodeposition of the next layer. The removal of this mold gives two adjacent permalloy/copper multilayered structures separated by a central trench. A new layer of photo resist is patterned to open the central trench and a final $Nickel_{80}$-$Iron_{20}$ layer is deposited covering the top of the electroplated layers and the inner walls of the trench. The photo resist is removed and copper is selectively etched using saturate Ammonium Hydroxide-Copper Sulfate solution. A free standing laminated NiFe core having several 1 μm thick NiFe layers separated by 1.5 micron air gaps is released from the wafer after the etch. The final NiFe layer is designed such that it

provides mechanical support to the structure while blocking the path for substantial eddy currents. Figure 2.1 shows the fabrication process steps and the final released structure.

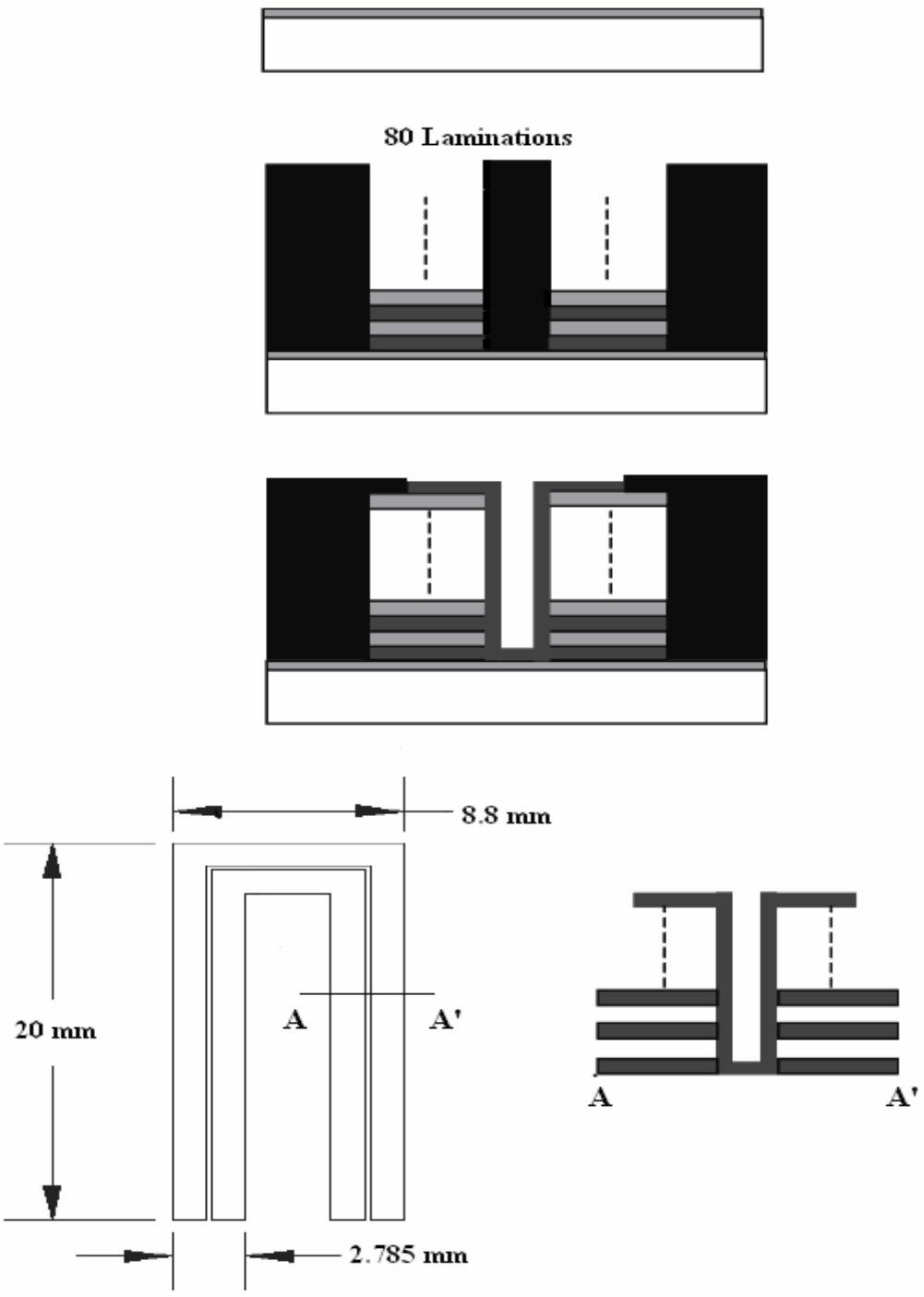

Figure 2.1 Fabrication Process for Inductor

2.2 Automated Electroplating System

An automated system was developed to carry out sequential electroplating of the magnetic and non-magnetic layers for core fabrication. Software using the National Instruments LabVIEW 7.1 graphical programming environment was developed to control the electroplating process. LabVIEW provides programming flexibility subject to hardware changes and allows rapid development of an application-based interface. Software and hardware integration allows the system to precisely control lamination thickness by monitoring the plating time and current. The control hardware and software are described in detail in this chapter.

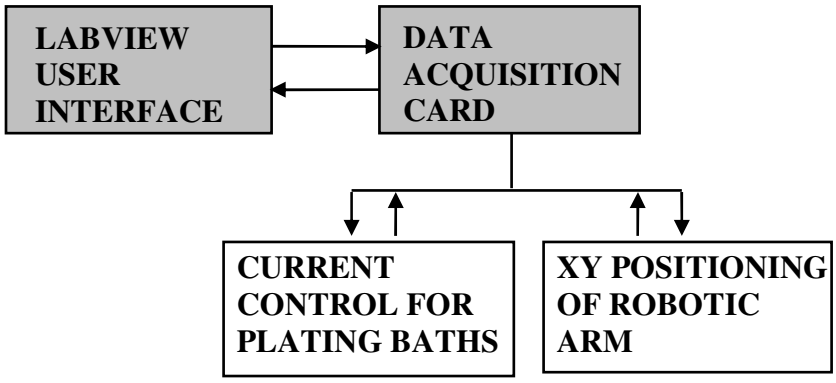

Figure 2.2 System level schematic of Automated Electroplating System

2.2.1 Hardware

The robot arm has two degrees of freedom and uses a stepper motor, DC motor and an optical sensor for a closed loop operation. The robot control hardware consists of a National Instruments PCI-6221 Data Acquisition card [12] , associated cable, position control and current control circuitry. Figure 2.3 shows the automated electroplating setup. A wafer holder attached to the robot arm carries the substrate to be electroplated on. The

stepper motor controls the lateral movement of the arm, allowing it to shuttle between electroplating baths and DI Rinse while the dc motor controls the transverse movement of the wafer into and out of each container.

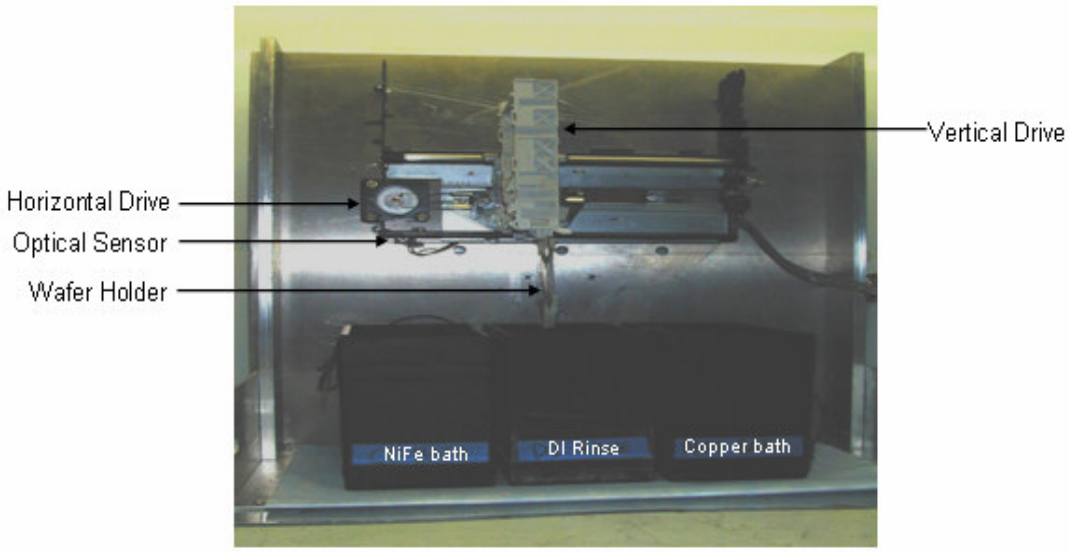

Figure 2.3 Automated Electroplating Robot

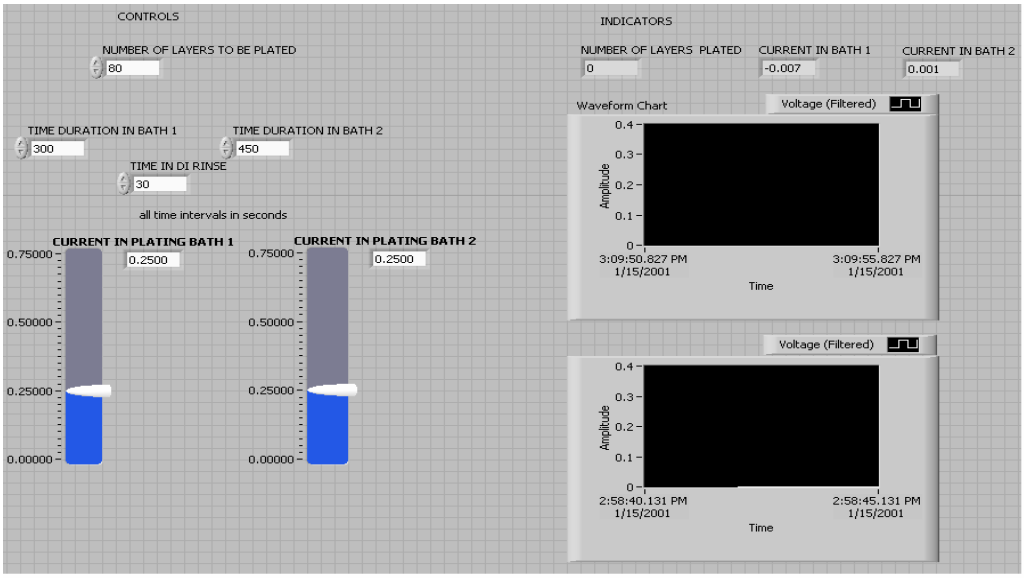

Figure 2.4 LabVIEW based User Interface

The graphical user interface allows the user to input parameters such as electroplating current, electroplating time and number of laminations required. Real time display of electroplating current and number of layers plated is also available as shown in figure 2.4.

2.2.1.1 Stepper Motor Control

SLA 7062M motor driver [13] operates the unipolar stepper motor for position control of the robotic arm. When the driver CLOCK input receives a step command signal from LabVIEW, the motor advances in the direction dictated by the signal level at the CW/CCW pin. The size of each step increment is set by the state of M1 and M2 which are both low in this case to achieve microstepping as small as sixteenth of a step for precise positioning.

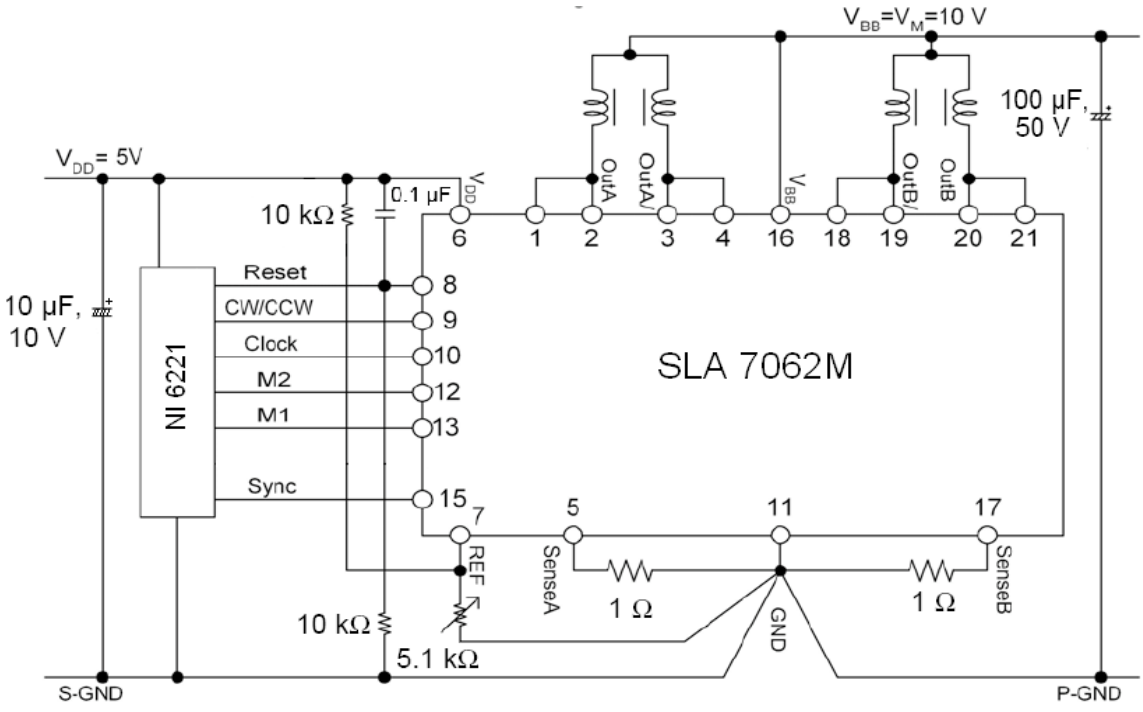

Figure 2.5 Stepper motor control circuit

2.2.1.2 DC Motor Control

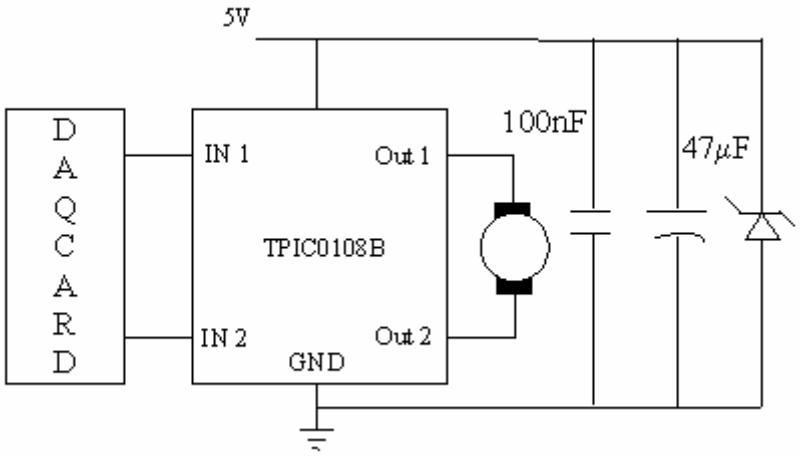

Figure 2.6 DC Motor Driver Circuit

TPIC0108B [14], a PWM control intelligent H-bridge is used for controlling the dc motor. The driver circuit receives TTL level signals from LabVIEW based on the direction of rotation required as shown in table 2.1 and thus provides smooth lowering and hoisting of the wafer in and out of the electroplating bath.

Table 2.2 H-Bridge Modes of Operation

IN1	IN2	Mode
0	0	Quiescent current supply mode
0	1	Clockwise
1	0	Counter Clockwise
1	1	Brake

2.2.1.3 Optical Sensor

The optical sensor CNZ1023 [15] consists of a light emitting diode and a phototransistor facing each other so that objects passing between them are detected. After each electroplating sequence, the arm moves back to the home position before starting the next cycle in order to prevent cumulative error in positioning. The sensor is positioned in the home location. When the arm is not in the home position, the signal level at the signal out pin is high as there is no obstruction to the light and the software commands the translator to move the stepper motor to home position. On reaching home position, the arm blocks the light transmission from the LED to the transistor and the signal level becomes low.

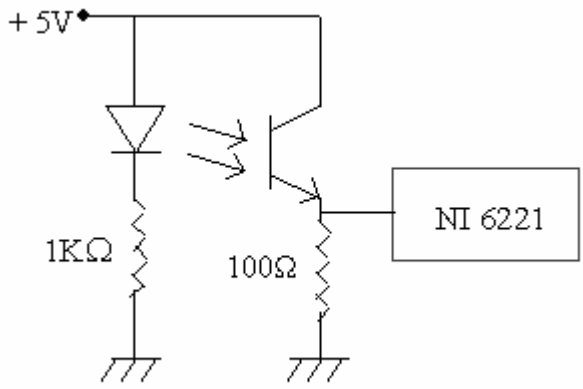

Figure 2.7 Optical sensor

2.2.1.4 Current Control

Each deposited NiFe or Cu layer adds resistance to the structure and hence, in absence of current control, for a fixed voltage source, the applied current for electrodeposition will gradually reduce. Since the plated thickness varies with the applied current density, current should be precisely controlled throughout the electrodeposition duration. Figure 2.8 shows a voltage source current controller with a closed loop. The operational amplifier LM358 compares the desired current with the

feedback current and corrects for the error in the output current by adjusting the gate voltage of the transistor T2. The feedback voltage is measured across a sense resistor of value 1 Ω in series with the plating bath.

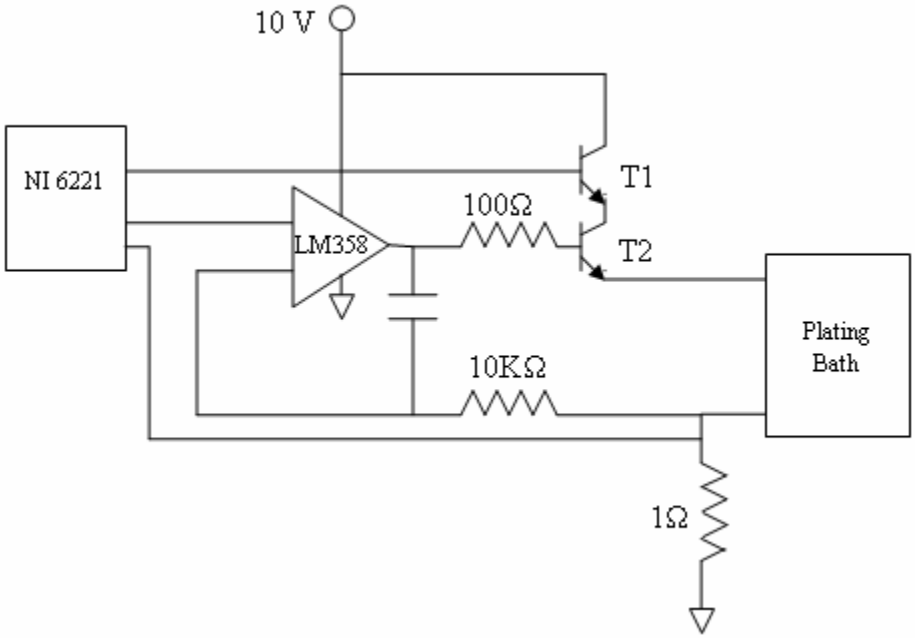

Figure 2.8 Voltage source current controller

2.2.2 Software

The LabVIEW Virtual Instrument (VI) sends command signals for driving the hardware circuitry and performs digital and analog data acquisition for monitoring, measurement and error correction. The flowchart in figure 2.9 gives an overview of the software developed for the automation of the electroplating process. Each VI block is described in detail in the Appendix.

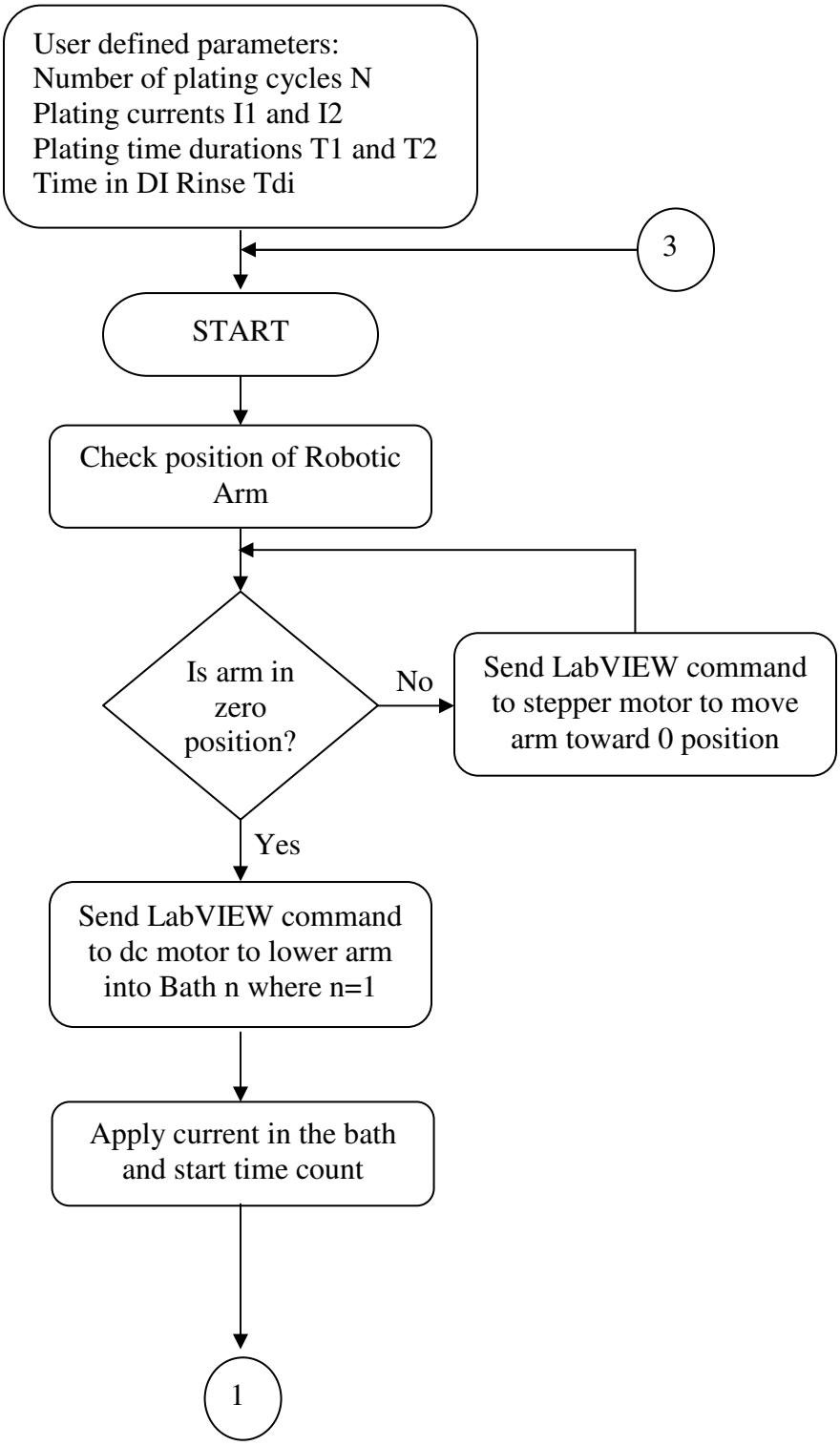

Figure 2.9 Flow Chart of Electroplating Process

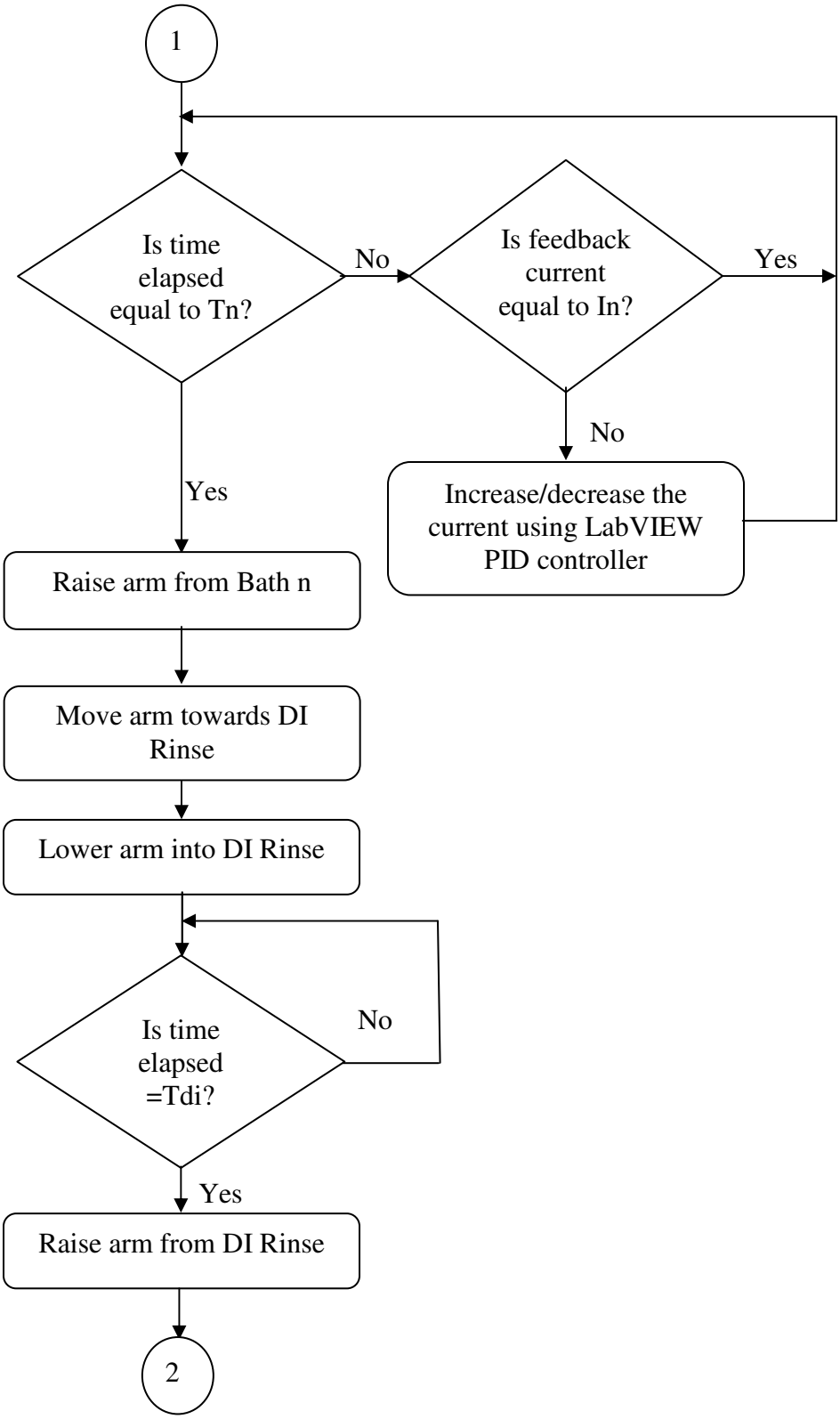

Figure 2.9 Flow Chart of Electroplating Process (Continued)

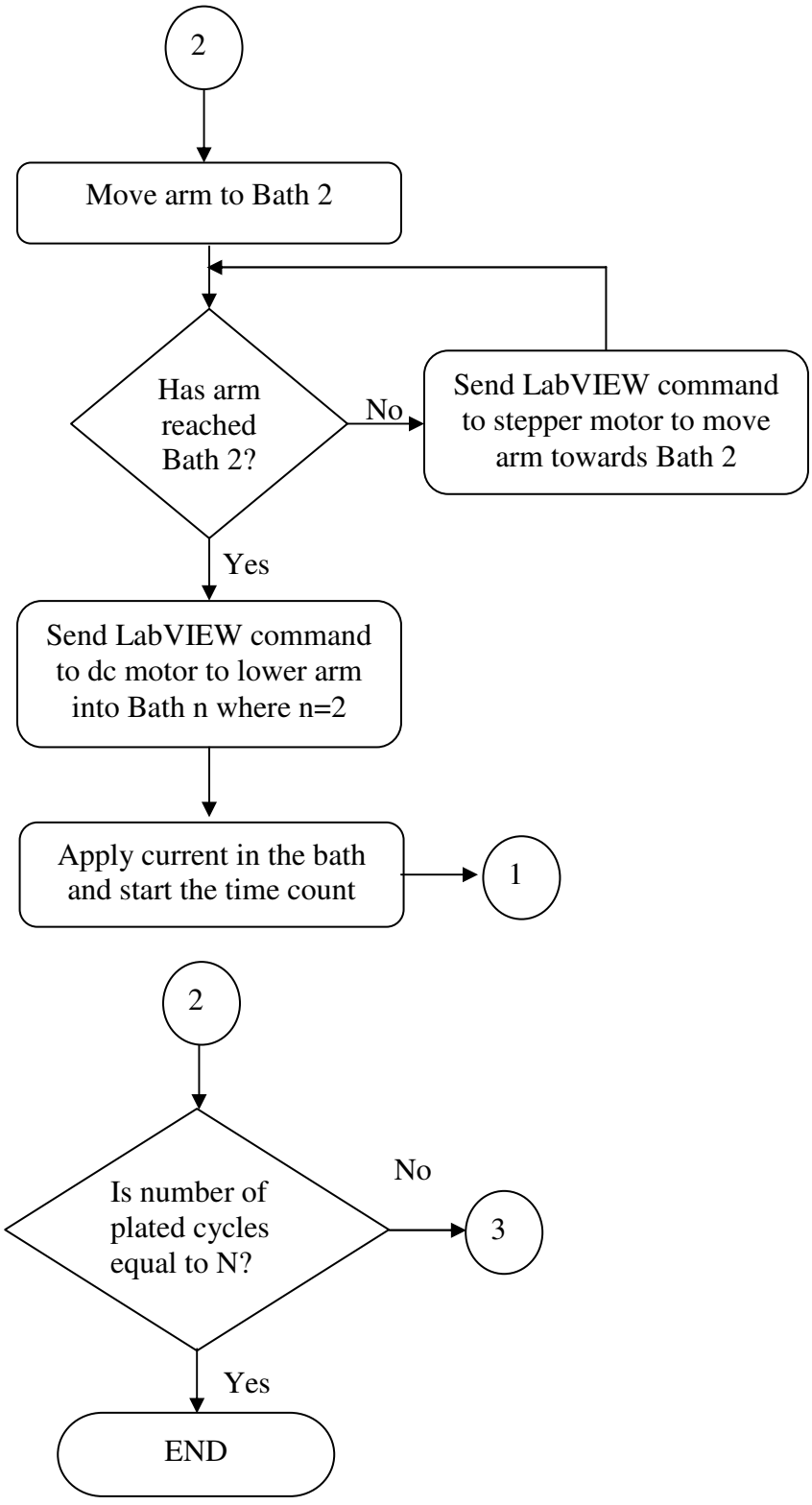

Figure 2.9 Flow Chart of Electroplating Process (Continued)

2.3 Future directions for Robot

Paddling mechanism of the robot arm can be incorporated as it has been shown to result in uniform NiFe plating [16]. The composition and reproducibility of the deposited films would also benefit from continuous monitoring of pH of the electrolyte and automatic addition of fresh iron to replace the depleted iron, acids and other agents. Though software (LabVIEW) has been used successfully to realize an electroplating robot, a microcontroller-based robot would be more reliable and less bulky. The current robot can only electroplate one wafer at a time. Fabrication of multiple cores at a time would make the process more efficient and cost effective.

2.4 Characterization of the fabricated inductor

A core fabricated using the automated electroplating process and having 80 laminations was hand wound with an insulated 36 AWG magnet wire for SEM measurement as shown in figure 2.10. To form the power inductor, three cores having 80 laminations each were stacked together and coated with enamel for insulation and the 600 μm stack was hand wound with a magnet wire of thickness 30 AWG to form 45 turns.

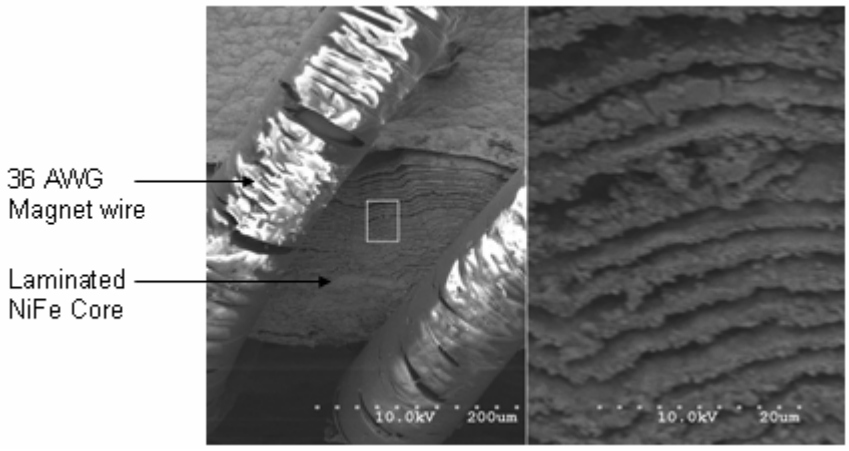

Figure 2.10 A side SEM showing 80 laminations of the core wound by a 36 AWG wire

The inductance and Q factor were measured using the impedance analyzer HP 4194 with the internal oscillation voltage set to 0.5 V peak to peak. The measured values are plotted in figure 2.11. The inductance has a maximum Q factor of 13.8 at 400 KHz and is greater than 7 between 35 kHz and 5 MHz. Self resonance occurs at a frequency higher than 40 MHz. The low frequency response of the inductor was measured using a Wayne Kerr 3245 precision inductance analyzer by superimposing a DC signal of 0.5 A on a 100mA AC signal. A soft saturation curve is obtained as shown in figure 2.12. The DC saturation current (I_{80}) is more than 0.5 A. The inductance at 0.5 A DC bias superimposed on a 300 KHz AC signal is 5.05 µH and the ac resistance is 400 mΩ.

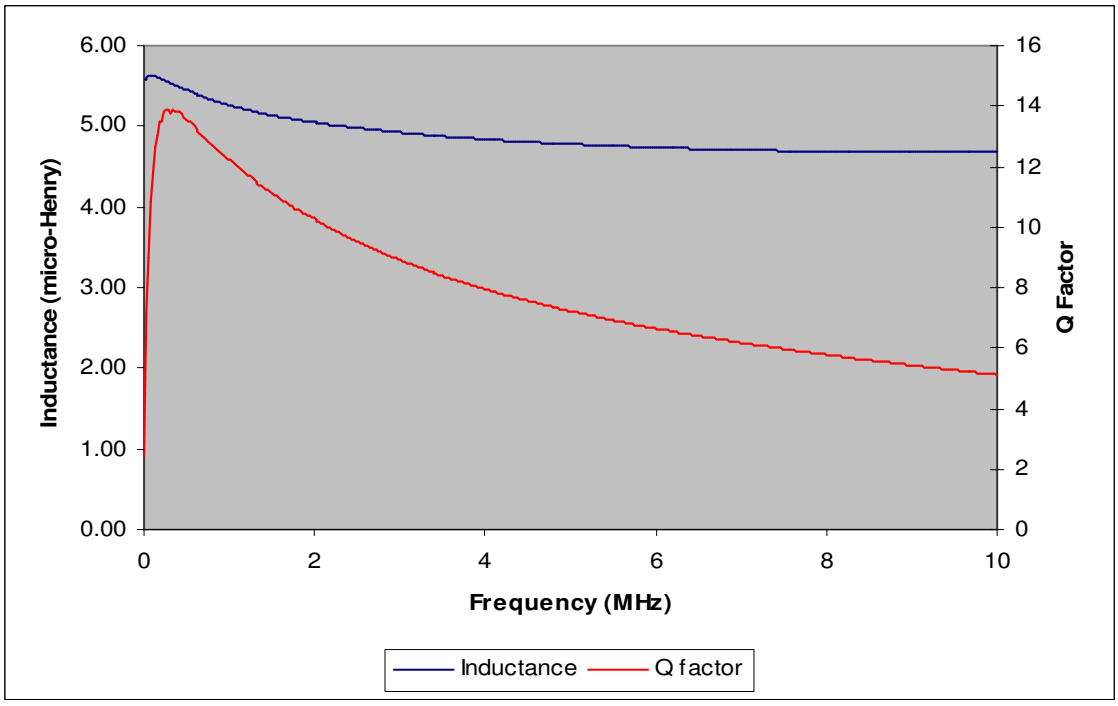

Figure 2.11 Measured inductance and Q factor of the inductor as a function of frequency

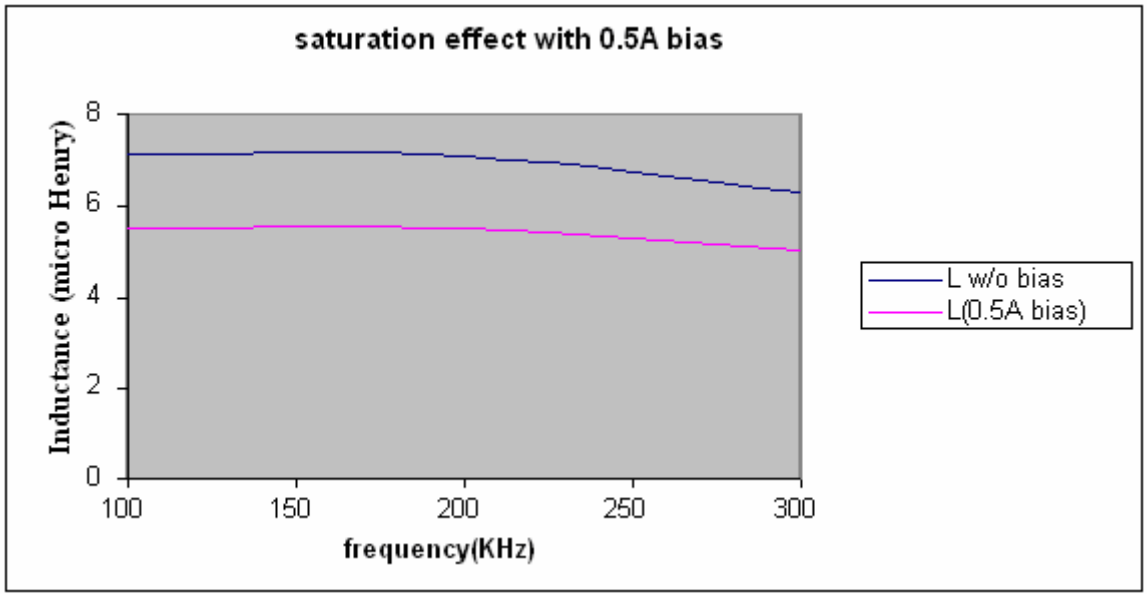

Figure 2.12 Measured inductance of the inductor as a function of frequency under DC bias

2.5 Summary for the inductor fabrication and characterization

Low profile stacked cores have been developed using CMOS compatible low temperature fabrication process. The automated electroplating system allows higher number of laminations compared to previous work and fabricated inductors having a higher inductance, Q factor and saturation current have been obtained using this technique.

CHAPTER 3: CHARACTERIZATION OF LAMINATED NiFe CORES

NiFe cores having micron thick laminations made using the copper etching technique explained in figure 2.1 have lower eddy current losses and higher Q compared to unlaminated cores. Previously, three different inductors with cores having 1 layer of 10 μm, 2 layers of 5 μm and 8 layers of 1.25 μm were fabricated and characterized for their frequency response [7]. In this chapter, test inductors with having thicker cores with higher number of laminations will be compared for their measured Q factor and resistance as a function of frequency.

3.1 Fabrication and characterization of test laminated cores

Four NiFe cores having different lamination thicknesses were fabricated using the same mask and plating current density as described in chapter 2.

Table 3.1 Details of the test cores

Core	Lamination Thickness (μm)	Number of Layers
A	61±0.1	1
B	0.8±0.1	70
C	2.3±0.1	35
D	1.1±0.1	70

After the laminated structures were released from the substrate, the composition of each core was measured by energy dispersion spectroscopy (EDS). The average

composition for cores A, C and D was Ni (86%) and Fe (14%) while the composition of core B was Ni (79%) and Fe (21%). The thickness of each lamination was measured from the side close up SEM of the cores and has been listed in table 3.1. The ± 0.1 μm tolerance is included for the error in SEM thickness measurement. Cores A and B have the same effective magnetic volume while cores C and D have the same effective magnetic volume.

3.2 Eddy Current Theory

In order to find the analytical solution for the inductance and resistance of a laminated core as a function of frequency, one-dimensional analysis of the magnetic flux distribution in a packet of laminations was carried out for the core model illustrated in figure 3.1. The derived equations are presented below for a core material having constant conductivity σ and fixed permeability μ as the vectors of electric and magnetic field vary harmonically with time at an angular frequency ω (rad/s). Detailed analysis is available in [17, 18] .

Under quasi-static conditions, the inductance Lo is given by

$$L_o = \frac{\mu w t N^2}{l} \tag{3.1}$$

where t is the total thickness of the core excluding the air gaps, *w* and *l* are the width and length of the core respectively and N is the number of turns of a winding that is uniformly wound around the laminated core.

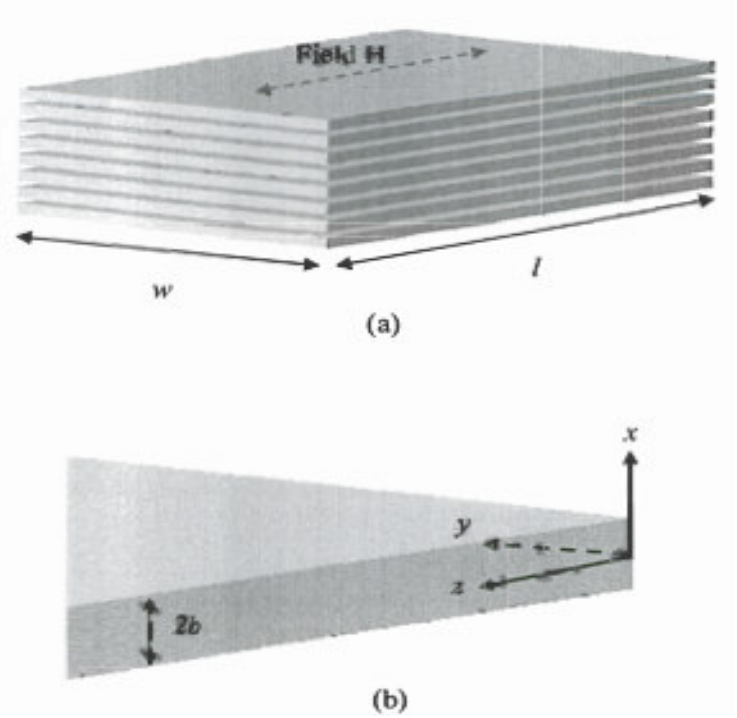

Figure 3.1 Core model (Assumptions: *l*>>*w* and *w*>>*2b*) [7, 17] (a) Packet of t/2b laminations with dimensions (b) A lamination of thickness 2b

As the frequency increases, skin depth δ in equation 1.6 decreases and the inductance is given by:

$$L_{ac} = L_o \frac{1}{\frac{2b}{\delta}} \times \frac{\sinh\frac{2b}{\delta} + \sin\frac{2b}{\delta}}{\cosh\frac{2b}{\delta} + \cos\frac{2b}{\delta}} \tag{3.2}$$

The resistance increases with frequency and is given by:

$$R_{ac} = \omega L_o \frac{1}{\frac{2b}{\delta}} \times \frac{\sinh\frac{2b}{\delta} - \sin\frac{2b}{\delta}}{\cosh\frac{2b}{\delta} + \cos\frac{2b}{\delta}} \tag{3.3}$$

For laminations of thickness 2b < δ/2, the change in inductance and resistance with frequency is very small.

$$L_{ac} \approx L_o \tag{3.4}$$

$$R_{ac} \approx \frac{\omega L_o}{6} \cdot \frac{2b}{\delta} = \frac{1}{3}\mu\sigma\omega^2 b^2 L_o \tag{3.5}$$

3.3 Characterization of the test inductors

After measurement of the lamination thickness, each core was coated with enamel to provide insulation and mechanical strength to the structure and hand-wound with insulated magnet wire of 32 AWG. The fabricated inductor is shown in figure 3.1. A calibration inductor having the same geometry and turns of coil but without the NiFe core, was used to characterize the winding resistance, skin effect in the coil and other parasitics which are not dependant on the core material.

3.3.1 Characterization of inductance as a function of frequency

Inductance of the A, B, C, D and no-core calibration inductor were measured using impedance analyzer HP4194A for different sinusoidal excitation amplitudes for a frequency sweep from 25 kHz to 10 MHz. Figures 3.3-3.7 show the inductance of the test inductors for oscillator voltage of 0.01V, 0.1V, 0.5V and 1V (RMS) that correspond to an RMS current of 0.2mA, 2mA, 10mA and 20mA respectively for frequency < 500 kHz since the impedance of the inductors is very small compared to the output impedance 50Ω of the impedance analyzer. The corresponding maximum magnetic field strengths of the test inductors are 0.181 A/m, 1.81 A/m, 9.099 A/m and 18.19 A/m.

In ferromagnetic materials, the magnetic permeability depends upon the amplitude and frequency of the excitation field [19]. For low excitation frequencies, the inductance increases with increase in AC excitation field due to the increase in effective permeability of electrodeposited NiFe. This effect is absent in the no core inductor.

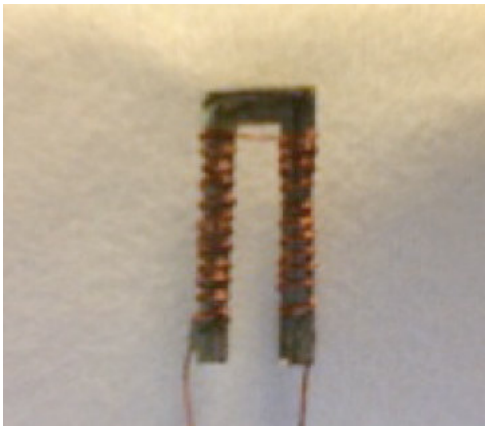

Figure 3.2 Fabricated test inductor using Core C

The inductance is almost independent of the excitation voltage at higher frequencies. The permeability of the cores could not be measured, so comparison of the measured inductance with the theoretically calculated value was not possible. However, assuming a long solenoid with 24 turns and a core having a relative permeability of 800 and resistivity of 17 μΩ-cm, a good fit is obtained between the measured and calculated inductance of inductor A. For inductor A, the skin depth of 60 μm occurs at a frequency of 18 kHz and the inductance rolls off beyond this frequency. The calculated inductance for inductor B matches the measured inductance at a much lower relative permeability of 140 and resistivity of 17 μΩ-cm of the core. This decrease in permeability could be due to the non uniformity in the composition of the electroplated nickel iron or increase in the coercivity with decrease in the film thickness. The skin depth for core B matches the lamination thickness at a frequency > 50 MHz and so the drop in inductance with increase in frequency is negligible in the lower MHz regime. For cores C and D, the inductance at 25 kHz is almost the same and matches the calculated value for a relative permeability of 190 and resistivity of 17 μΩ-cm but as the lamination thickness of D is

half of that of C, the inductance for D remains more constant over the frequency range compared to C. The skin depth of cores C and D matches the lamination thickness at a frequency of 25 MHz and 50 MHz respectively but a fall in the inductance is seen prior to this frequency in both cases potentially due to the shorts between the laminations created by the residual copper that was not completely etched during the wet etching process. The resistivity calculated from the eddy resistance separated from the measured resistance of the laminated cores in section 3.3.2 using equation 3.5 is 1-3 μΩ-cm, which is an order of magnitude less than the assumed resistivity due to the lamination shorts. The inductance of an inductor having a U shaped core may not be justified by the long solenoid formula so the assumed value of the relative permeability and resistivity may be erroneous but the decrease in the permeability with decrease in lamination thickness can still be explained.

Figures 3.8 and 3.9 show the saturation characteristics of the test inductors A and B measured using 3245 Wayne Kerr precision inductance analyzer at an AC excitation current of 100mA with a variable DC offset. The DC saturation current of inductor B exceeds 700 mA but is around 400 mA for inductor A.

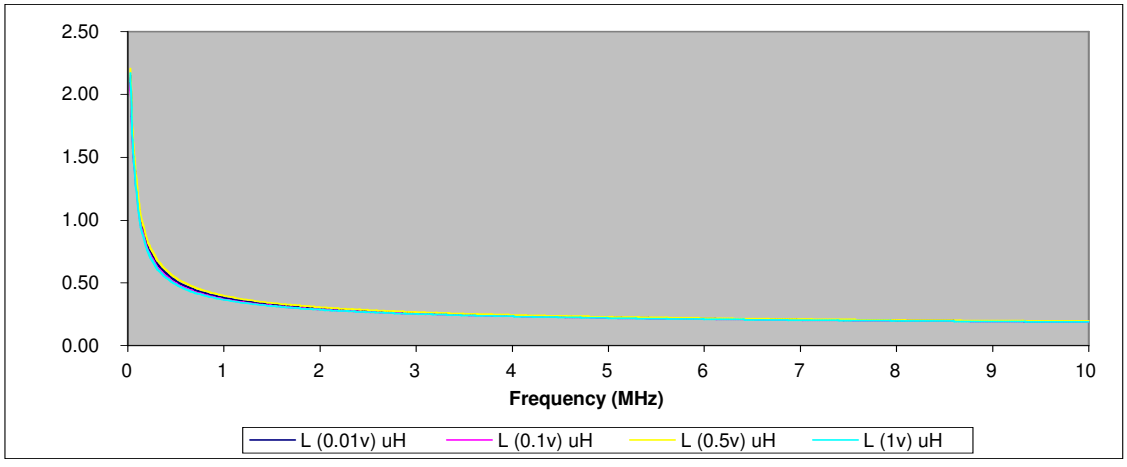

Figure 3.3 Inductance of inductor A as a function of frequency and excitation voltage

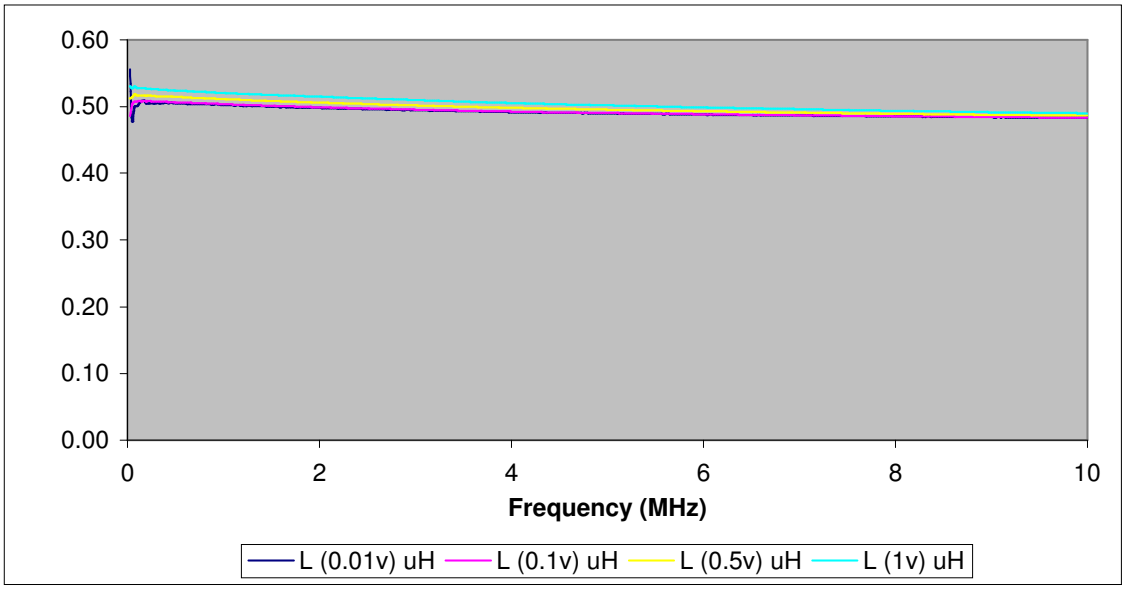

Figure 3.4 Inductance of inductor B as a function of frequency and excitation voltage

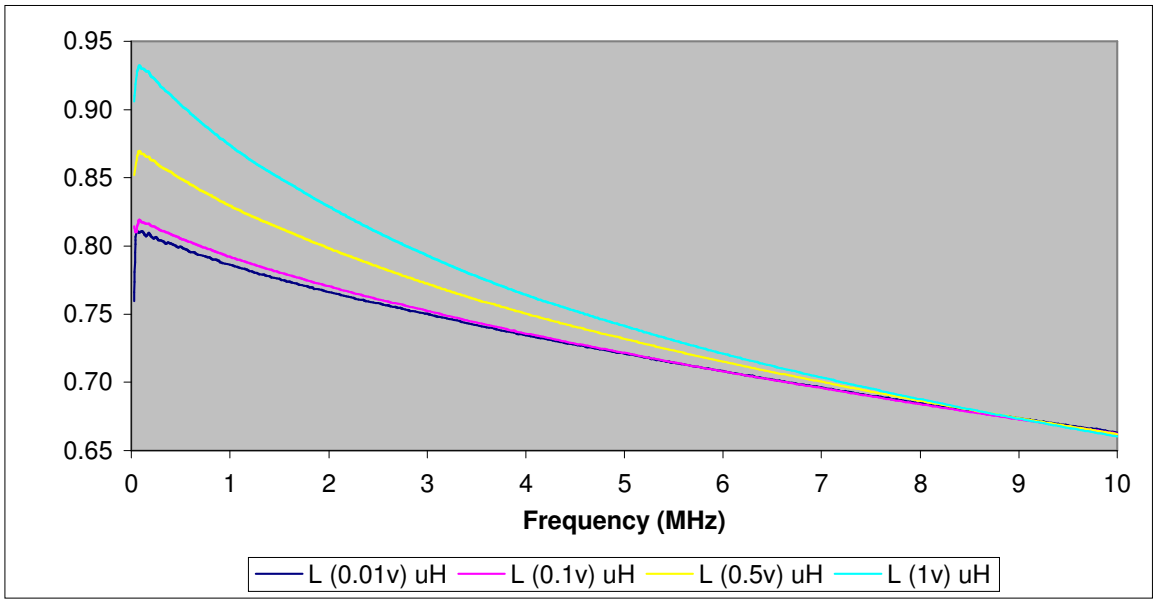

Figure 3.5 Inductance of inductor C as a function of frequency and excitation voltage

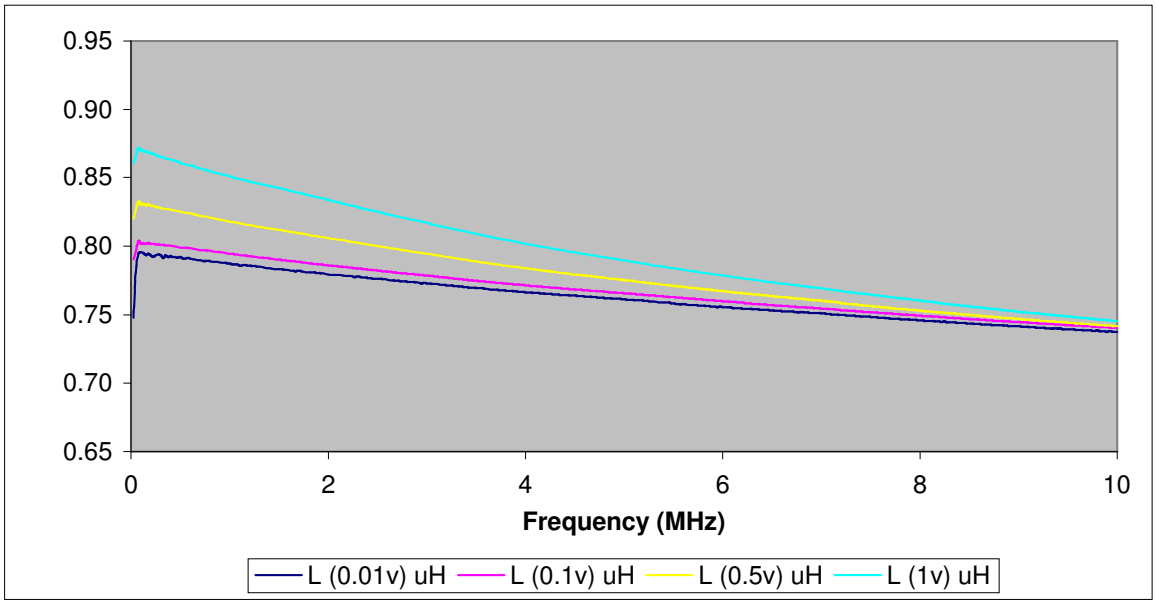

Figure 3.6 Inductance of inductor D as a function of frequency and excitation voltage

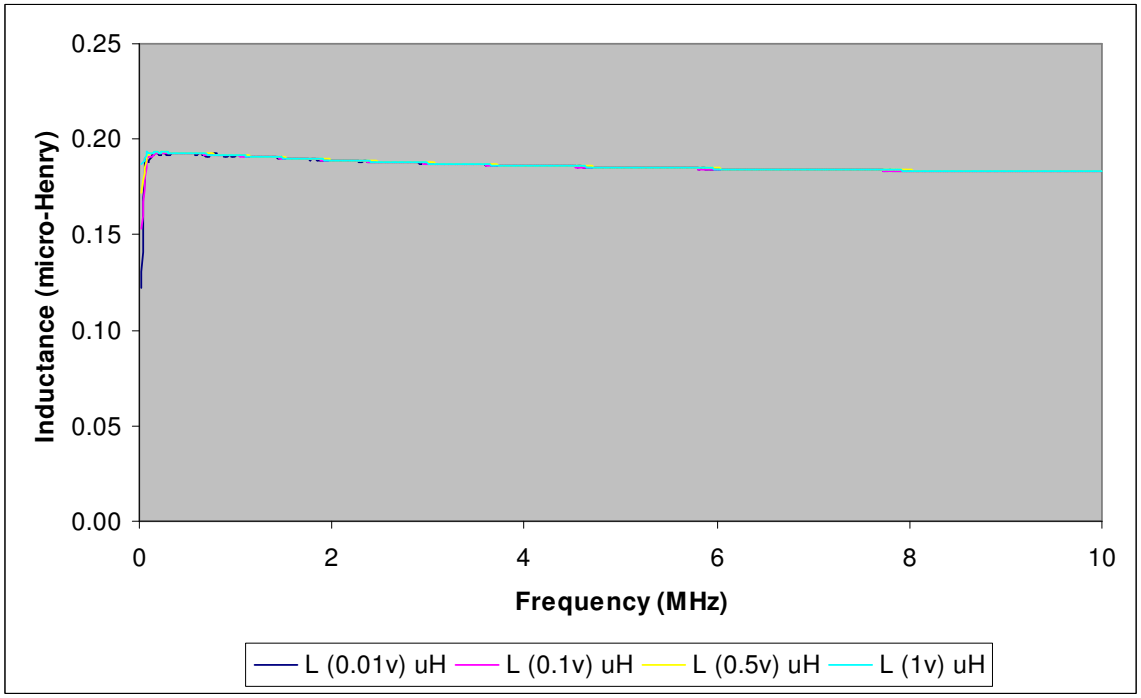

Figure 3.7 Inductance of no core inductor as a function of frequency and excitation voltage

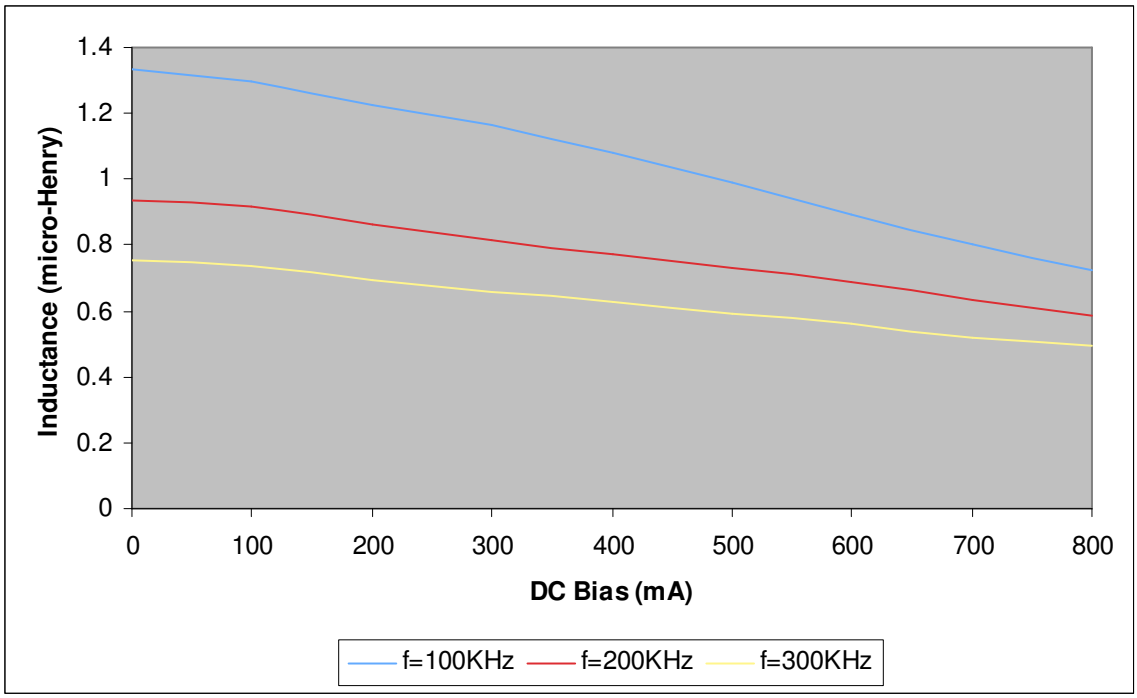

Figure 3.8 Saturation characteristics of inductor A

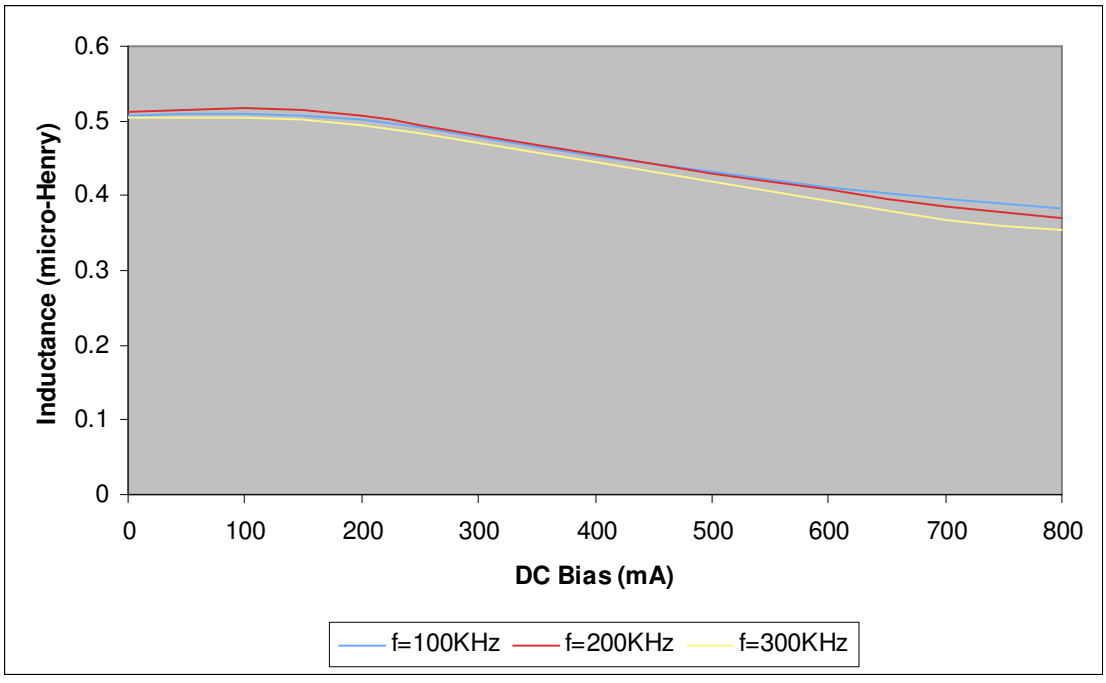

Figure 3.9 Saturation characteristics of inductor B

3.3.2 Resistance characterization

Magnetic core losses arise due to Joule heating from electric currents induced in the material by the changing magnetization. The core losses can be separated into three portions: the static hysteresis loss, the classical eddy current loss and the excess eddy current loss also referred to as anomalous losses [20].

The core energy loss per cycle is measured from the BH curve obtained by applying an alternating magnetic field to the core. The hysteresis losses can be separated from the dynamic losses (classical eddy loss + excess eddy current loss) by running a DC hysteresis curve at the same magnetic field amplitude as used to attain the induction level for the AC curve on a hysteresis graph [21] or by quasi-static hysteresis loop measurement [22]. The area thus obtained is independent of the AC field and can be subtracted from the AC hysteresis loop area to obtain the field dependent term referred to as the dynamic energy loss. The classical eddy current losses are calculated for a homogenous material with no magnetic domain structure and are a function of the square of the magnetization frequency while the excess eddy current loss arises from magnetic domain-wall dynamics with scales on the order of microstructural features and are proportional to the 3/2 power of the magnetization frequency [22]. For a core subjected to sinusoidal excitation and having a uniform magnetic field, the core losses are given by [23] :

$$P_{core} = P_h + P_{classicaleddy} + P_{excess}$$

$$= a \cdot f + b \cdot f^2 + c \cdot f^{\frac{3}{2}} \qquad (3.6)$$

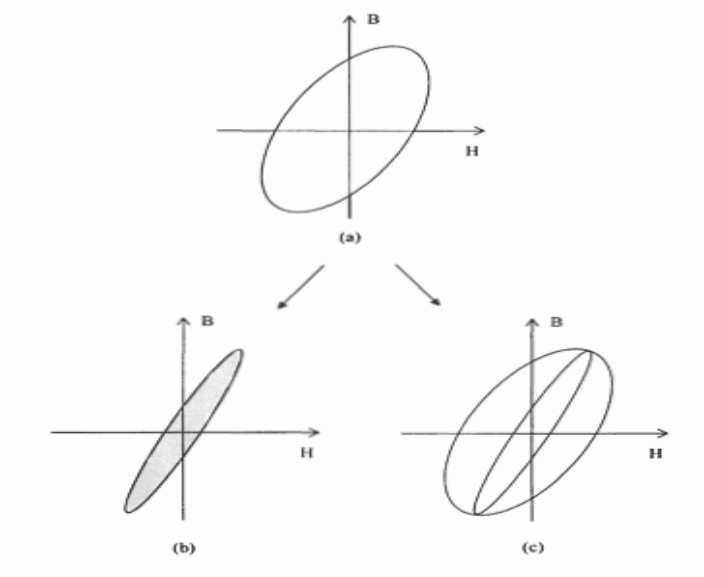

Figure 3.10 (a) AC Hysteresis Loop measured at high frequency (b) Quasi-Static Hysteresis Loop (c) dynamic loop added to the quasi-static hysteresis loop area [7]

Equation 3.7 can be rewritten in terms of the core resistance as:

$$R_{core} = R_h + R_{classicaleddy} + R_{excess} = C_h \cdot f + C_{ed} \cdot f^2 + C_{ex} \cdot f^{\frac{3}{2}} \tag{3.7}$$

where R_{core} is the resistance of the test inductor core after subtracting the resistance of the no core inductor to discount the effect of winding resistance and C_h, C_{ed} and C_{ex} are the hysteresis loss coefficient, eddy current loss coefficient and excess loss coefficient respectively. Curve fitting was done using the asymptote method described in [7] and confirmed with MATLAB to find the coefficients of the core resistance measured at an effective RMS excitation voltage of 0.1V for cores A-D. Table 3.2 lists the coefficients of the core resistance for the frequency range mentioned in the table.

Table 3.2 Coefficients of Core Resistance

Core	Frequency (Hz)	C_h	C_{ed}	C_{ex}
A	25K-50K	3.8E-06	1.95E-11	4.01E-09
B	25K-3M	2.6E-08	1.35E-14	1.30E-11
C	25K-3M	1.9E-07	1.30E-13	1.29E-11
D	25K-3M	8.0E-08	7.40E-14	2.62E-12

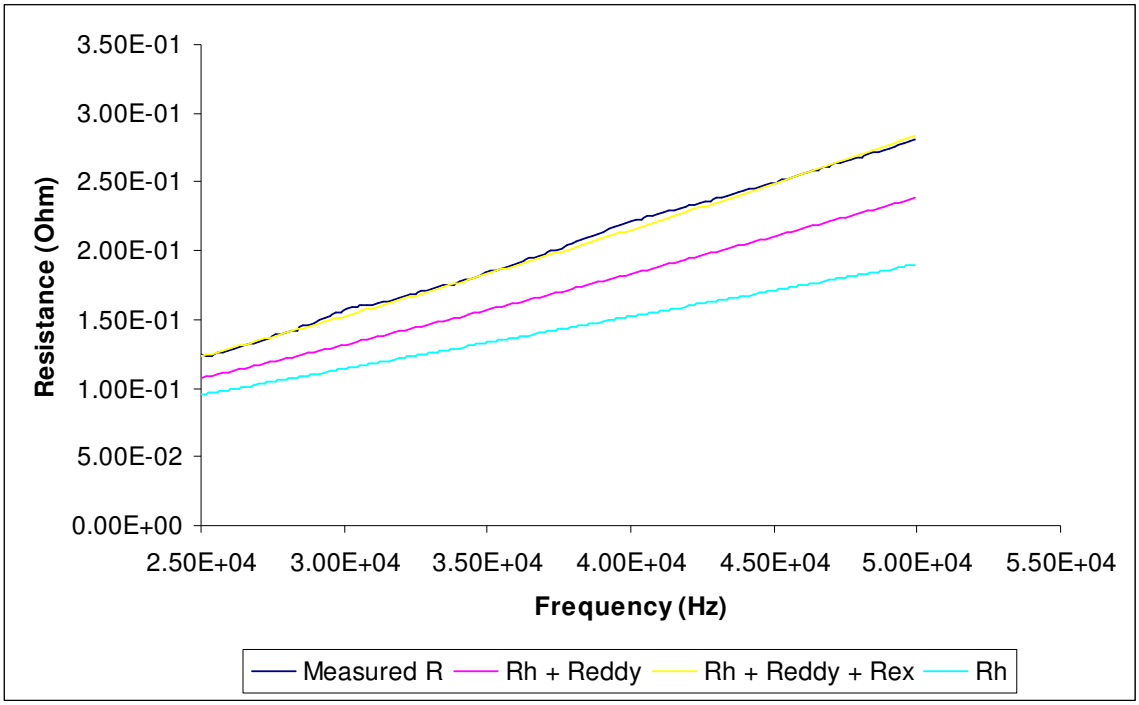

Figure 3.11 Measured and separated resistances by curve fitting for core A

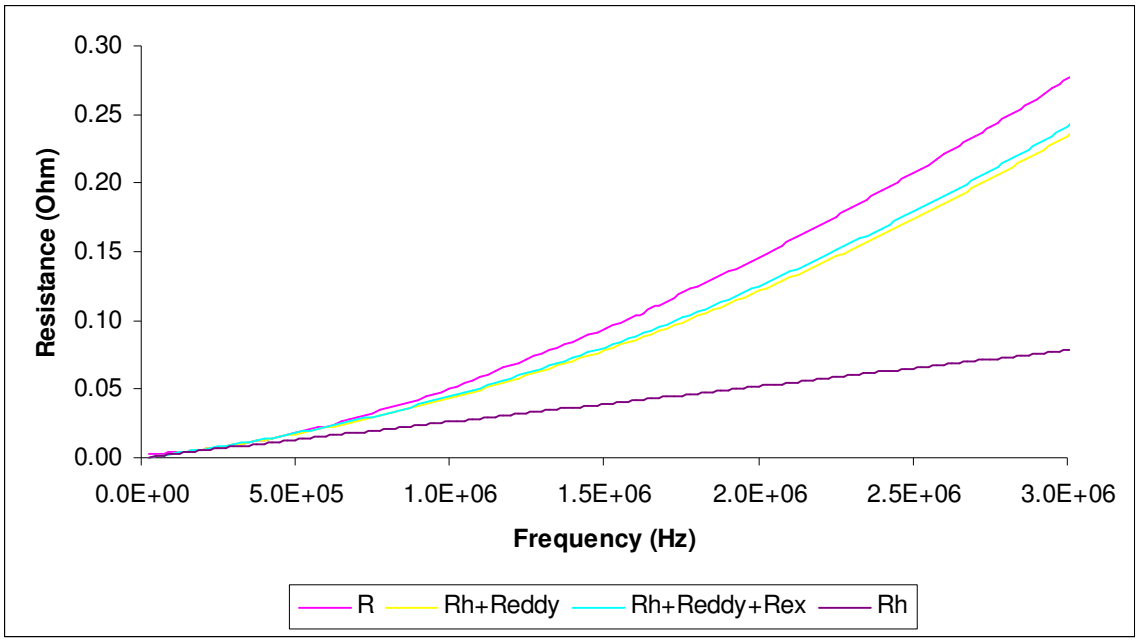

Figure 3.12 Measured and separated resistances by curve fitting for core B

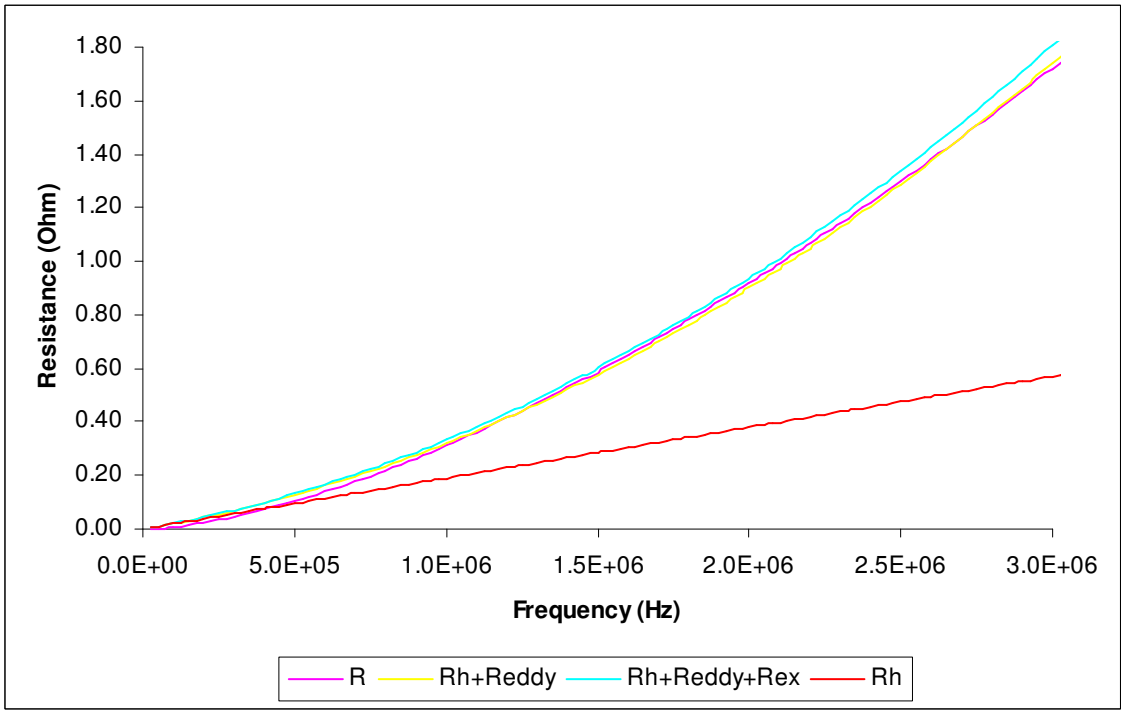

Figure 3.13 Measured and separated resistances by curve fitting for core C

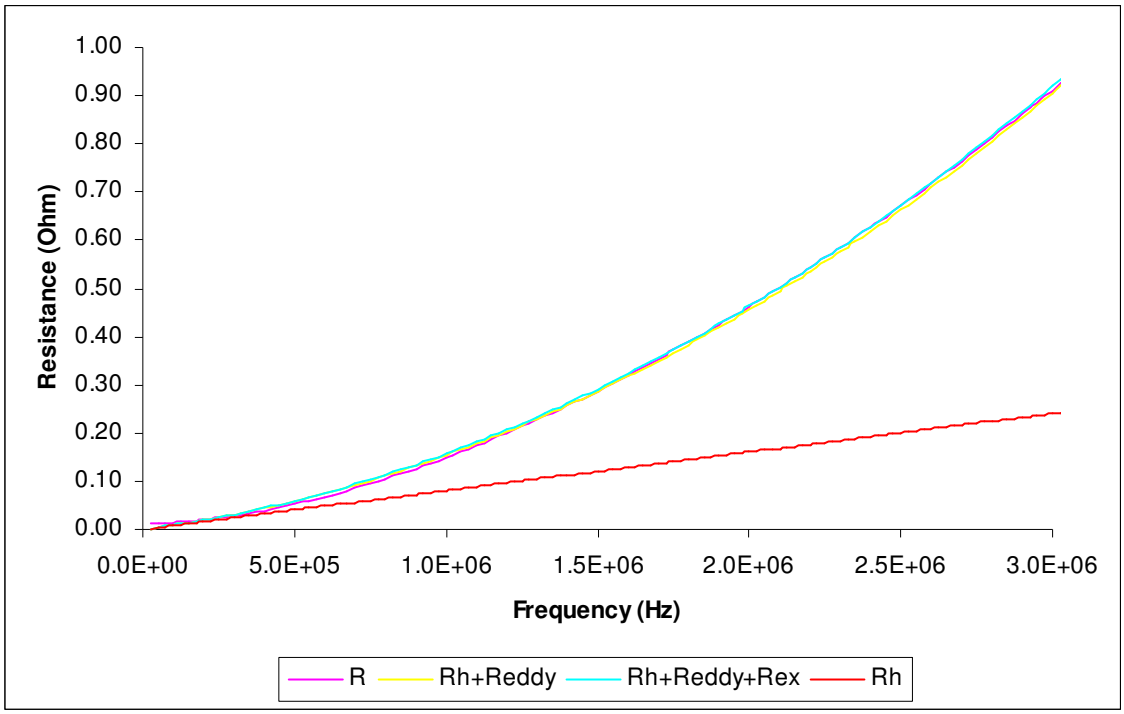

Figure 3.14 Measured and separated resistances by curve fitting for core D

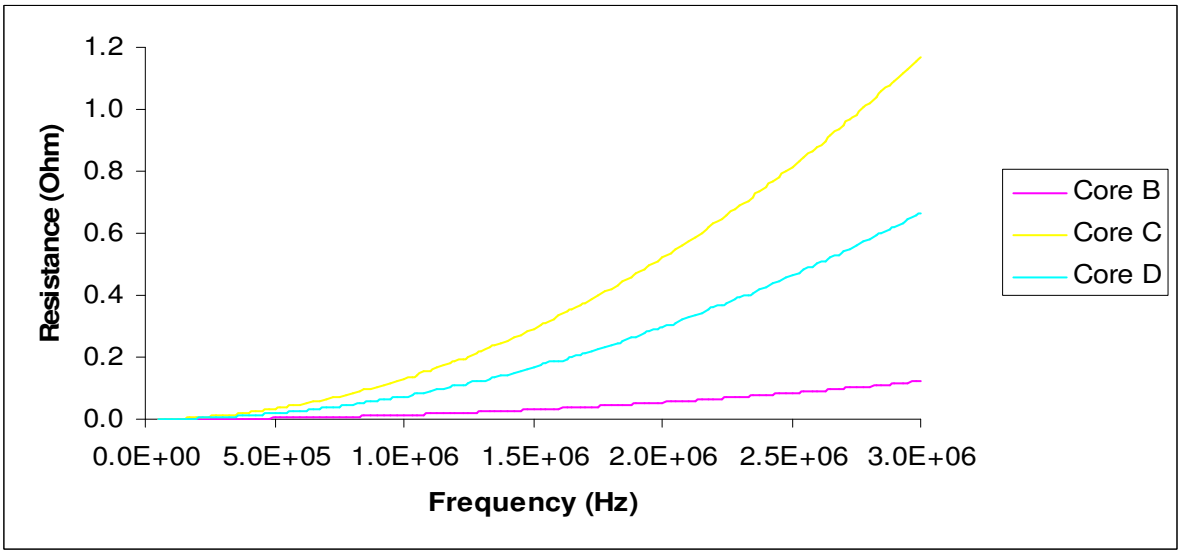

Figure 3.15 Eddy resistances of different test cores

Figures 3.11-3.14 show the separated resistances for the different test cores. The eddy resistance is independent of the size or shape of the core and only depends on the lamination thickness, assuming the resistivity and permeability of the core material remain constant with change in lamination thickness. Figure 3.15 compares the eddy resistances of cores B, C and D. Core A has the highest eddy losses among all four cores due to lack of laminations while Core B has the lowest eddy losses because of its submicron laminations. It is clearly observed that the excess eddy current losses are almost negligible compared to hysteresis and classical eddy losses in all four cases.

3.3.3 Q factor characterization

Figure 3.16- 3.19 shows the measured Q factor of the inductors as a function of frequency and excitation voltage. Inductor B has the highest Q factor (maximum of 21 at 0.01 V rms excitation) among the four test inductors. At lower frequencies (<500 KHz), the Q factor is independent of the excitation voltage level. For frequencies in the lower MHz regime, the Q factor dependence on excitation voltage is the highest and goes on decreasing as the frequency pushes into the higher MHz regime. The Q factor behavior with change in excitation voltage and frequency can be explained by separating it into three different components.

$$\frac{1}{Q_{inductor}} = \frac{1}{Q_{wire}} + \frac{1}{Q_{hysteresis}} + \frac{1}{Q_{dynamic}} \tag{3.8}$$

where Q_{wire}, $Q_{hysteresis}$ and $Q_{dynamic}$ are the Q factors calculated using R_{nocore}, $R_{hysteresis}$ and $R_{dynamic}$ respectively.

The separated Q factors for cores C and D at an excitation voltage of 0.1V rms are shown in figure 3.20 and 3.21. At lower frequencies, the hysteresis and eddy losses are

very small and the winding resistance dominates. Hence, in the lower frequency range, Q_{wire} is the major contributor to $Q_{inductor}$ and change in Q factor with excitation voltage is negligible. As the frequency increases, hysteresis losses become the dominant losses and the Q factor becomes dependent on the level of excitation voltage. In the higher MHz regime (>2MHz), the eddy losses are dominant as they are proportional to f^2. Increase in the eddy resistance and decrease in the inductance with frequency causes the Q factor to decrease. Since the eddy resistance is not a function of the excitation voltage, the change in Q factor with excitation voltage becomes very small at high frequencies. The Q factor of inductor A does not follow the above behavior. As the thickness of core A is very large compared to its skin depth at frequencies > 200 KHz, the eddy losses dominate and should cause the Q factor to fall. This effect is negated by the portion of the core that does not contain NiFe and acts like an air-cored inductor shunted across the NiFe cored inductor.

$$Q_{effective} = Q_{inductor} + Q_{air} \tag{3.10}$$

In spite of the decrease in $Q_{inductor}$ with increase in eddy losses, Q_{air} increases with increase in frequency and $Q_{effective}$ increases until the self-resonance frequency is reached. This effect is seen in inductors B, C and D at frequencies greater than 10MHz.

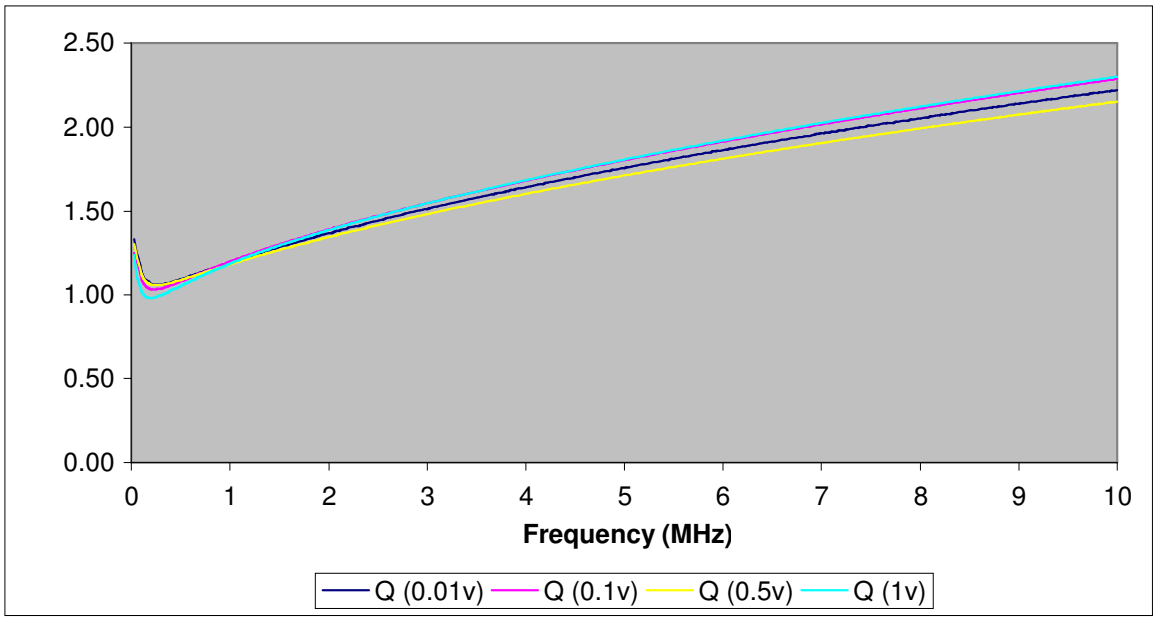

Figure 3.16 Q factor of inductor A measured at different excitation voltages

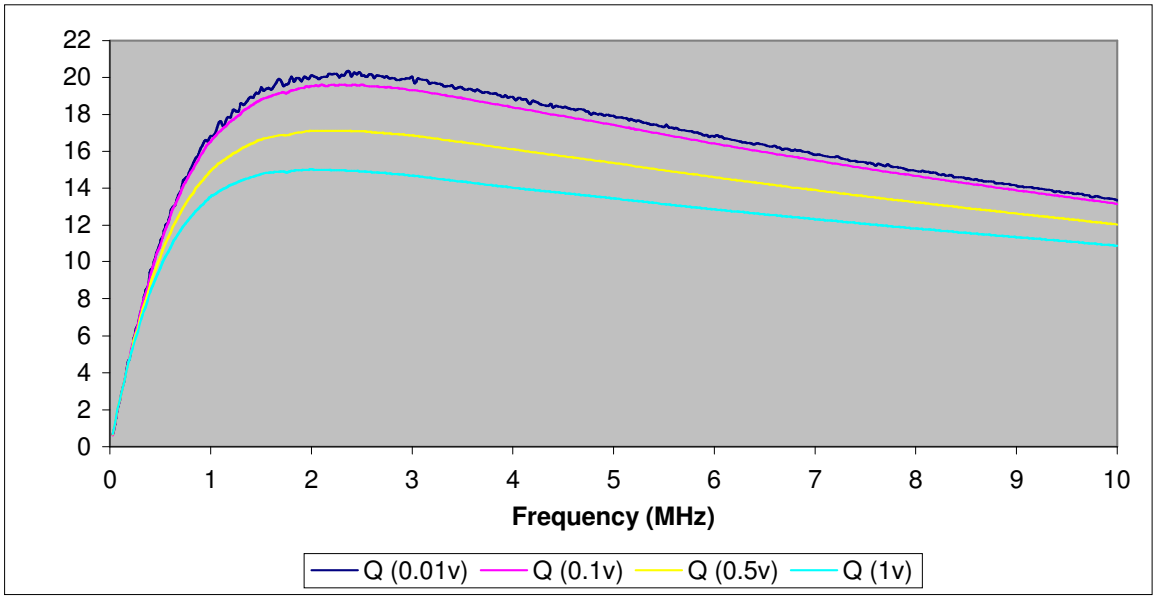

Figure 3.17 Q factor of inductor B measured at different excitation voltages

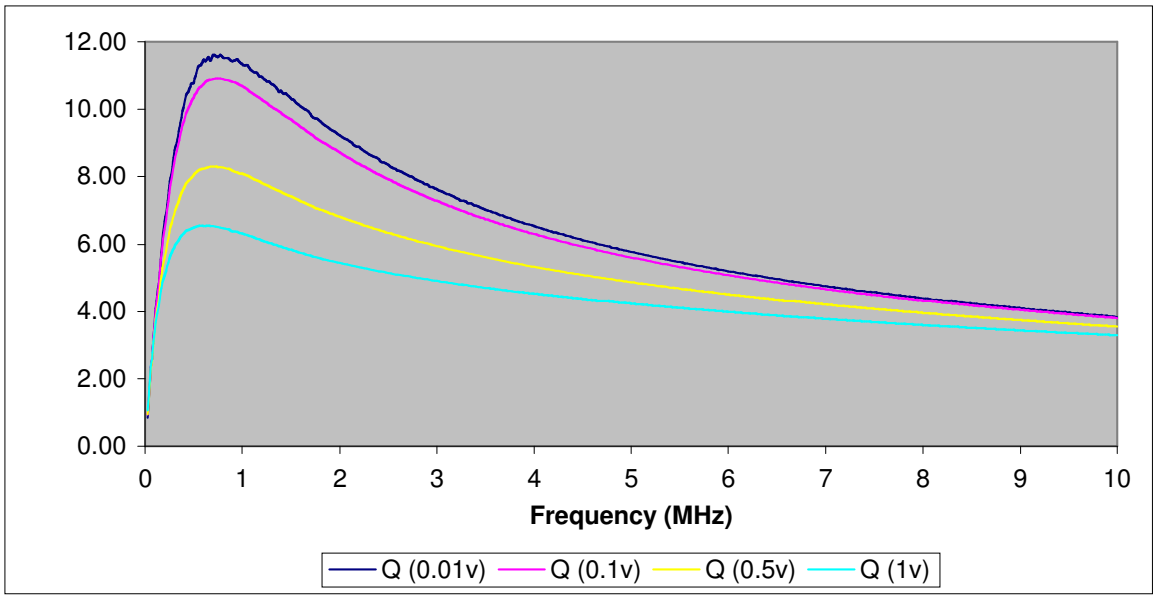

Figure 3.18 Q factor of inductor C measured at different excitation voltages

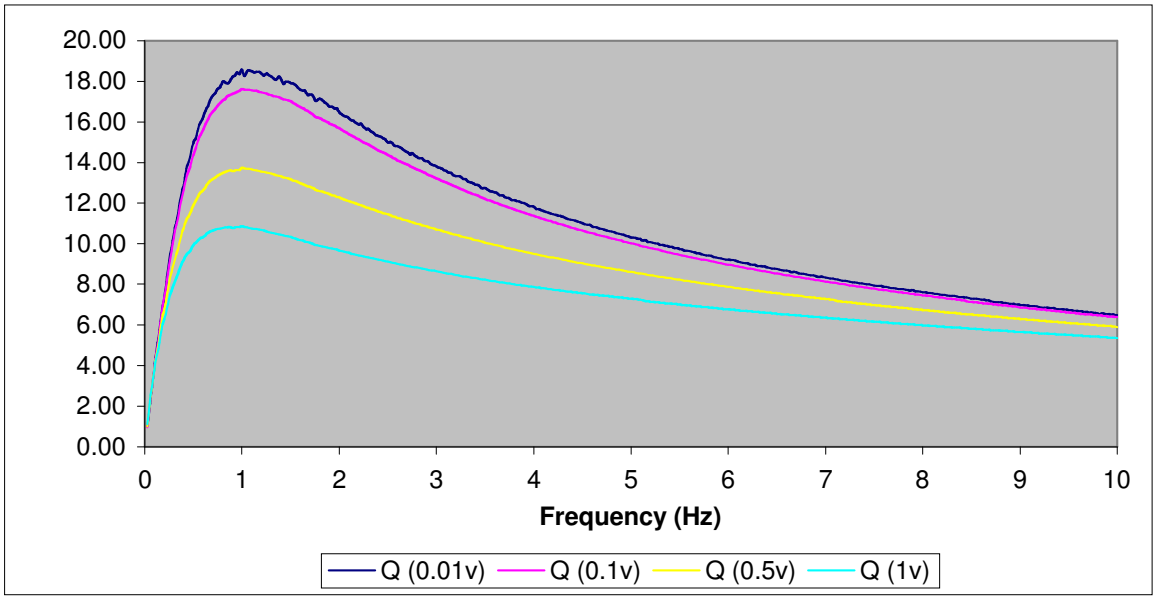

Figure 3.19 Q factor of inductor D measured at different excitation voltages

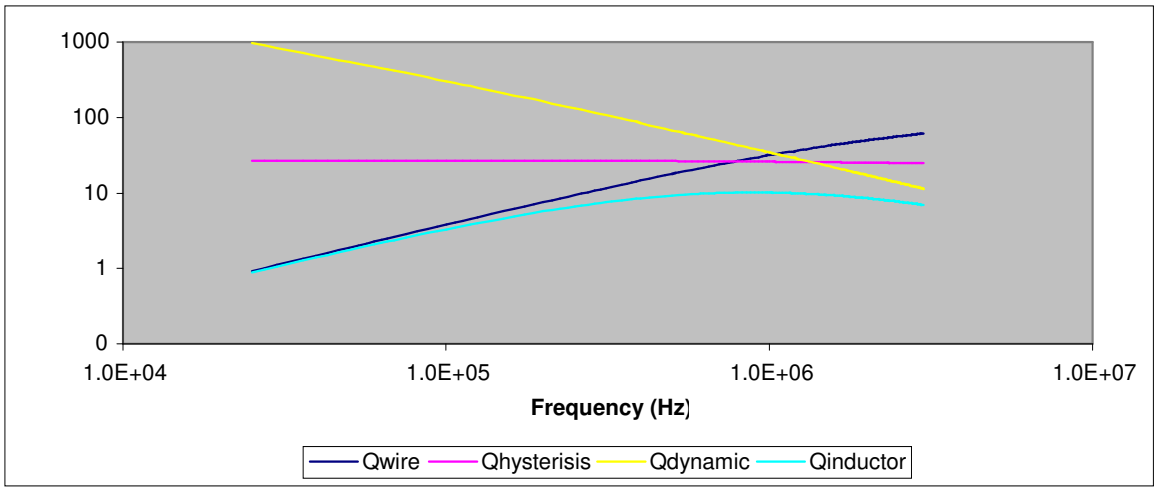

Figure 3.20 Measured and separated Q factors of inductor C measured at 0.1V

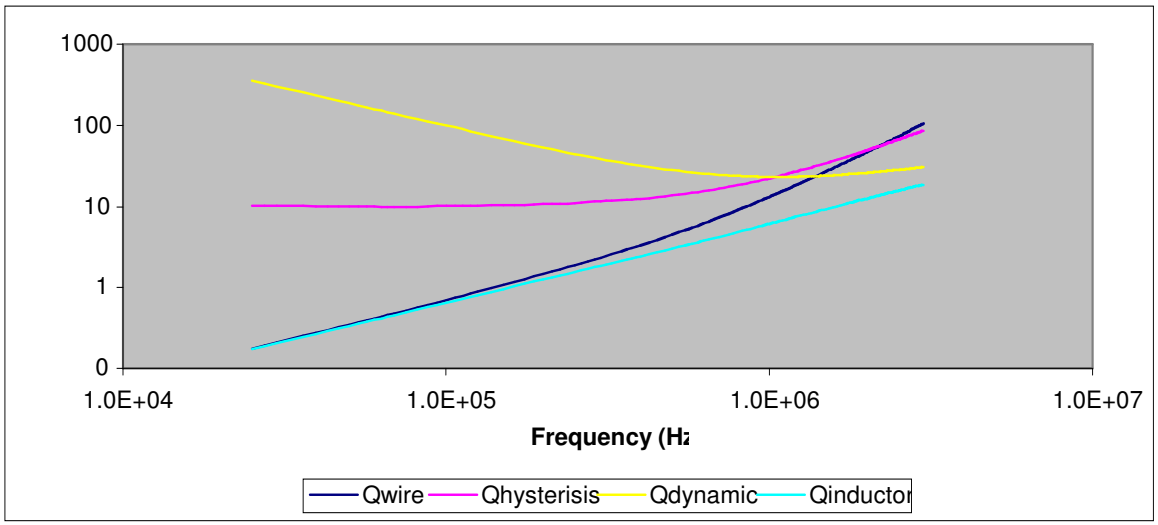

Figure 3.21 Measured and separated Q factors of inductor D measured at 0.1V

3.4 Summary

Four test inductors with different lamination thicknesses were fabricated and characterized for their inductance, Q factor and resistance as a function of frequency and excitation voltage. It was found that core D, having submicron laminations achieved by the automated electroplating process, has the most desirable L, Q and R behavior over the

frequency sweep. Decreasing the thickness of laminations decreases the eddy losses and hence gives better performance of the inductor for the same volume.

CHAPTER 4: DEMONSTRATION OF HIGH POWER DC-DC BUCK CONVERTER

Conventional DC-DC switch mode converters made by discrete component assembly have higher performance than their linear counterparts but are bulky by modern packaging standards. Increasing the switching frequency allows the use of smaller magnetic components. Miniaturized DC-DC converters are generally rated at an internal switching frequency of around 500 kHz [24] but designs have been realized for higher switching frequencies [6]. Inductors with electroplated Ni-Zn ferrite films having high dc saturation current have been used to demonstrate miniaturized converters operating at 5 MHz but the low relative permeability of 100-110 limits the use of the inductors to 1-3 Watt devices [25]. The highest power conversion at high frequency in miniaturized converters has been reported in [26]. A high efficiency (>82%) 10-Watt class buck converter operating at 2 MHz has been demonstrated using planar inductors using highly resistive ($\rho > 10^5 \Omega$ m) NiZn ferrite thin plates. The effective volume of the planar inductor is slightly higher than the inductor fabricated for this research but the thickness of the planar inductor is almost twice the thickness of the highly laminated inductor. The process is not ideal for batch manufacturing and integrated fabrication with other power conversion components. In this research, DC-DC switch-mode regulator with buck topology operating at 2MHz and power conversion of >10W has been demonstrated. Though the converter has been built using discrete components, the low temperature CMOS compatible fabrication process of the inductor makes it very suitable for hybrid microcircuit manufacturing to get smaller footprint and noise.

4.1 Basics of Buck Converter

Buck voltage converters produce an average output voltage lower than the input source voltage. A basic buck topology using ideal components has been illustrated in figure 4.1. The inductor serves as a current source to the output load impedance. In the continuous conduction mode, the switch Q1 is turned on at time t=0 and the diode becomes reverse biased. The current flowing through the inductor causes a positive voltage drop V_L across it, which in turn causes the inductor current i_L to increase linearly from I1 to I2. At $t=t_1$, Q1 is off and due to the stored inductive energy, the inductor current now flows through the free-wheeling diode and to the load, inducing a negative voltage drop across L, which in turn causes the inductor current to decrease gradually from I2 to I1. At time $t=t_2$, the cycle repeats itself as Q1 is turned on again for the next time period.

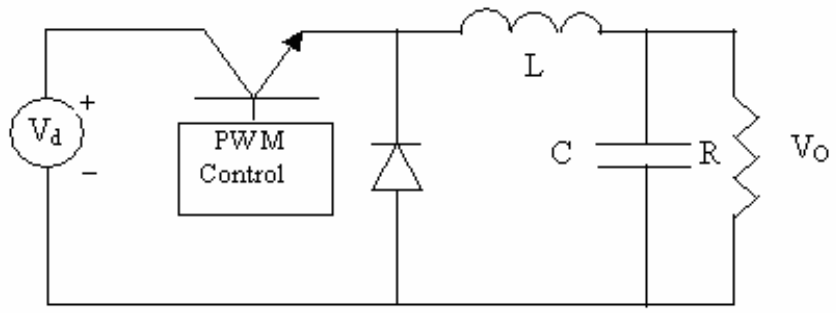

Figure 4.1 DC-DC Buck Converter Circuit

Assuming that V_d, V_o and L are constant and there is no initial current,

During charging,

$$V_L = V_d - V_0 = L\frac{I_2 - I_1}{t_1} = L\frac{\Delta I_L}{t_1} \tag{4.1}$$

Or $$t_1 = \frac{L\Delta I_L}{V_d - V_o} \tag{4.2}$$

During discharging,

$$V_L = -V_0 = L\frac{\Delta I_L}{t_2} \tag{4.3}$$

Or $$t_2 = \frac{L\Delta I_L}{V_o} \tag{4.4}$$

The integral of inductor voltage over one time period (t_1+t_2) must be zero.

$$\int_0^{t_1} (V_d - V_o)dt + \int_{t_1}^{t_2} (-V_o)dt = 0$$

Using t_1=DT and t_2=(1-D)T, where D is the duty ratio and T is the period of the switching,

$$(V_d - V_o)t_{on} = V_o(T - t_{on})$$

$$\frac{V_o}{V_d} = \frac{t_{on}}{T} = D \tag{4.5}$$

The average output voltage, V_o, is inversely proportional to D.

The switching period T is

$$T = \frac{1}{f} = t_1 + t_2 = L\Delta I\frac{V_d}{(V_d - V_o)V_o} \tag{4.6}$$

Or $$\Delta I_L = \frac{(V_d - V_o)V_o}{fLV_d} = \frac{V_d D(1-D)}{fL} \tag{4.7}$$

The output capacitor acts as a low-pass filter, reducing the output voltage ripple as a result of the fluctuating current ΔI_L through the inductor.

$$i_c(t) = C\frac{dv_c(t)}{dt}$$

From time t=0 to t=t_1, the capacitor C charges and the average capacitor current is I_c=I_o. The peak-to-peak capacitor ripple voltage ΔV_c is

$$\Delta V_c = v_c(t_1) - v_c(0) = \frac{1}{C}\int_0^{t1} I_c dt = -\frac{I_o t_1}{C} \tag{4.8}$$

$$t_1 = \frac{V_d - V_o}{V_o f} \tag{4.9}$$

Increase in operating frequency leads to reduction of inductor current ripple ΔI_L and size of the filter components L and C reducing the overall dimensions of the converter board. The above calculations do not take into account various non-idealities that affect the performance of the buck converter. Losses in the windings, MOSFET, diode, ESR loss in the input and output capacitors, inductor core losses, printed circuit board copper loss reduce the efficiency of the converter [27].

1) Inductor DCR loss:

The worst-case average power loss due to the series resistance R_{DC} associated with L is given by

$$P_{DCR\ RMS} = \left(I_{OUT_{MAX}} + \sqrt{2}\Delta I_L\right)^2 R_{DC}^2 \tag{4.10}$$

The equation shows that R_{DC} should be as small as possible to achieve low power loss and better efficiency.

2) Switching losses:

The power loss in the MOSFET occurs due to the MOSFET on-resistance and switching losses. Commutation losses occur in the switches during the on-off transitions. As the operating frequency increases, the increase in switching losses leads to lower efficiency. Switching at zero voltage or zero current can significantly reduce these losses [28].

3) Diode losses

Most buck converters today are synchronous buck converters, replacing the diode with an FET. Although requiring more components and additional switch logic sequencing, this topology ensures faster switch turn-on time and lower FET series resistance compared to the diode. The freewheeling diode in parallel with the FET would still contribute some losses during the reverse recovery period. A Schottky diode is used to reduce the losses.

Worst-case diode loss is

$$P_{DIODE} = \left(1 - \frac{V_{OUT}}{V_{IN_{MAX}}}\right) I_{OUT_{MAX}} V_D \tag{4.11}$$

where V_D is the voltage drop across the diode (0.3V for a Schottky diode) at the given output current $I_{OUT_{MAX}}$.

To investigate the effect of the effective series resistance of the inductor on the converter performance, a lumped resistance R_L accounting for the inductor winding and core losses is inserted in series with L.

The diode current I_d is equal to I_L when the switch is on and zero when the switch is off. Therefore the average input current is

$$I_d = DI_L \tag{4.12}$$

The average inductor current is

$$I_L = \frac{V_o}{R} \tag{4.13}$$

To maintain the volt-second balance during t_{on} and t_{off} ,

$$(V_d - V_o - I_d R_L) t_{on} = \left(V_o + (1-D) I_L R_L\right) \cdot (T - t_{on}) \tag{4.14}$$

Using equations 4.12 - 4.14 to solve for the output voltage of the converter,

$$V_o = \frac{DV_d}{\left(1 + \frac{R_L(1-2D^2)}{R}\right)} \tag{4.15}$$

This equation includes the correction factor for the series resistance of the inductor as compared to the ideal converter.

Efficiency of the converter is the ratio of the output power and the input power.

$$\eta = \frac{V_0 I_L}{V_d I_d} \tag{4.16}$$

Using equations 4.12-4.15 to solve 4.16,

$$\eta = \frac{1}{1 + \frac{R_L}{R}\left(1-2D^2\right)} \tag{4.17}$$

As the duty ratio increases, efficiency of the buck converter increases as predicted by equation 4.16.

4.2 DC-DC Buck Converter operating at 2MHz

To demonstrate the application of the micromachined laminated power inductors developed in this work, the fabricated inductor introduced in chapter 2.3 has been utilized in a compact DC-DC buck converter module. The discrete components used in the module have been listed in table 4.1. The schematic of the converter module is shown in figure 4.2. The converter has a fixed output voltage of 12V and a switching frequency of 2MHz [29]. To measure the efficiency of the module under different load conditions, the input current and output voltage were measured for a fixed input voltage and different load resistor values.

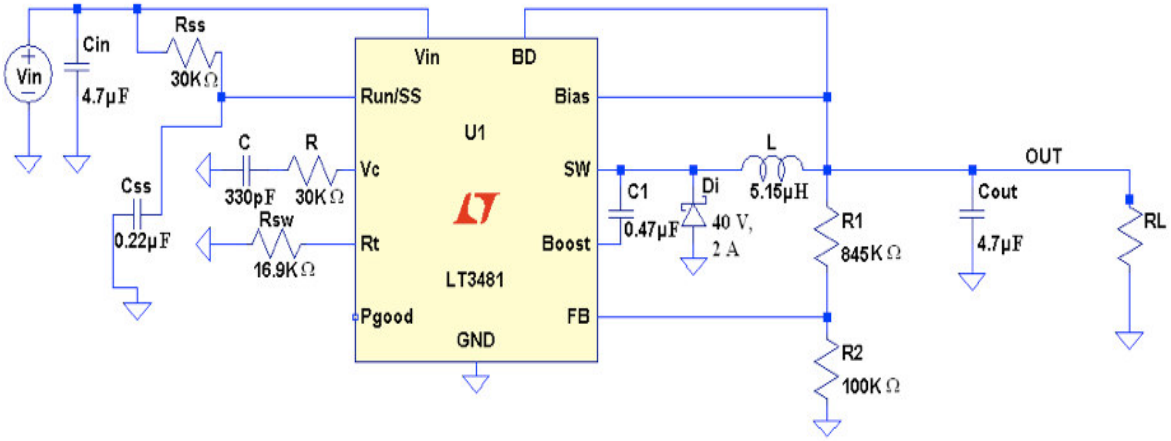

Figure 4.2 Schematic of the DC-DC buck converter

Table 4.1 Converter components

Components Used	Details
Power inductor	Laminated core having 240 layers of 1 µm thickness each Inductance of 5.15 µH at 2 MHz Q of 10.1 at 2MHz
Step Down Switching regulator	LT3481 Maximum current: 2A Maximum operating frequency: 2.8 MHz
Discrete electronic components	Resistors, input and output capacitors, schottky diode with surface mount packaging for low profile converter module

Figure 4.3 shows the output voltage and efficiency of the converter for a fixed input voltage of 20V. The output voltage is maintained within 1% regulation for output

power ≤ 6W and within 2% regulation for output power ≤ 11.8W. The efficiency is greater than 78% for all load conditions from 2.2W to 11.8W. Linear Technology simulation tool LTspice/ Switcher CAD was used to compare the actual performance of the converter module with the simulated performance. Simulations were carried out at different values of inductor effective series resistance to get the closest fit for efficiency. A series resistance of 2Ω gives efficiency close to the measured efficiency at a load condition of 9.27W.

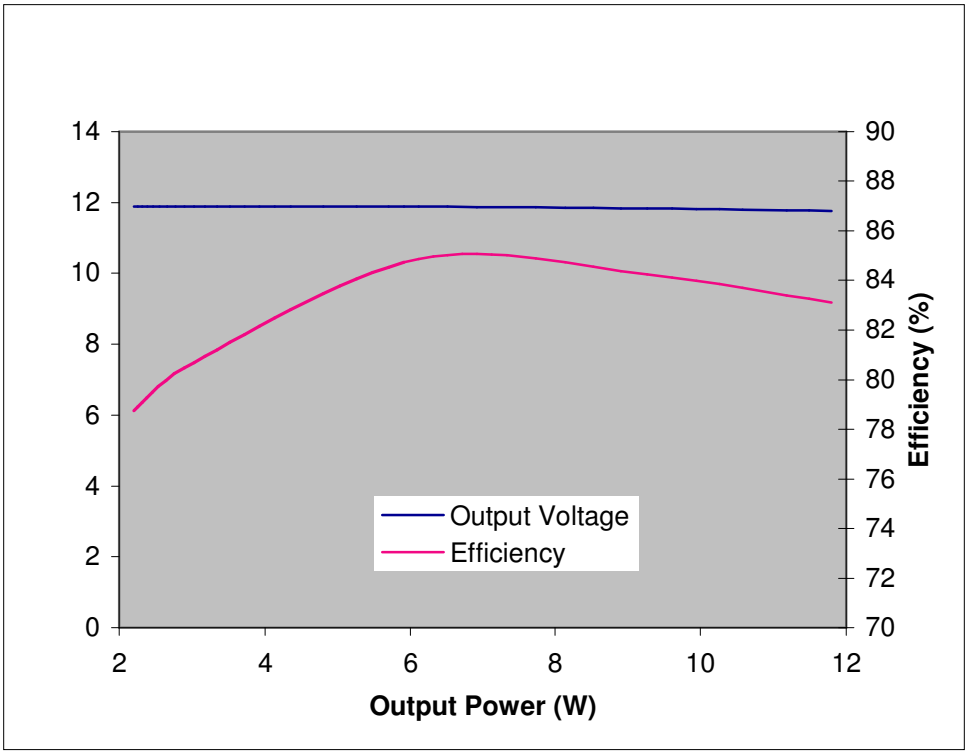

Figure 4.3 Output voltage and Efficiency of the converter at different load conditions for input voltage of 20V

Efficiency calculated from equation 4.17 using R_L of 2Ω is 96.4% as compared to the measured efficiency of 84.25% for the same load condition. This discrepancy arises as losses such as the high switching losses in the MHz operating regime are neglected in the theoretical calculation. The resistance corresponding to the losses cannot always be

lumped as a series resistance with the inductance in the model. This assumption can also lead to erroneous results.

Figure 4.4 shows the performance of the converter for an input voltage of 25V. As depicted by equation 4.17, the efficiency is less compared to the efficiency for an input voltage of 20V. The output voltage and efficiency fall rapidly for output current higher than 0.8 A as the inductor core starts to saturate magnetically.

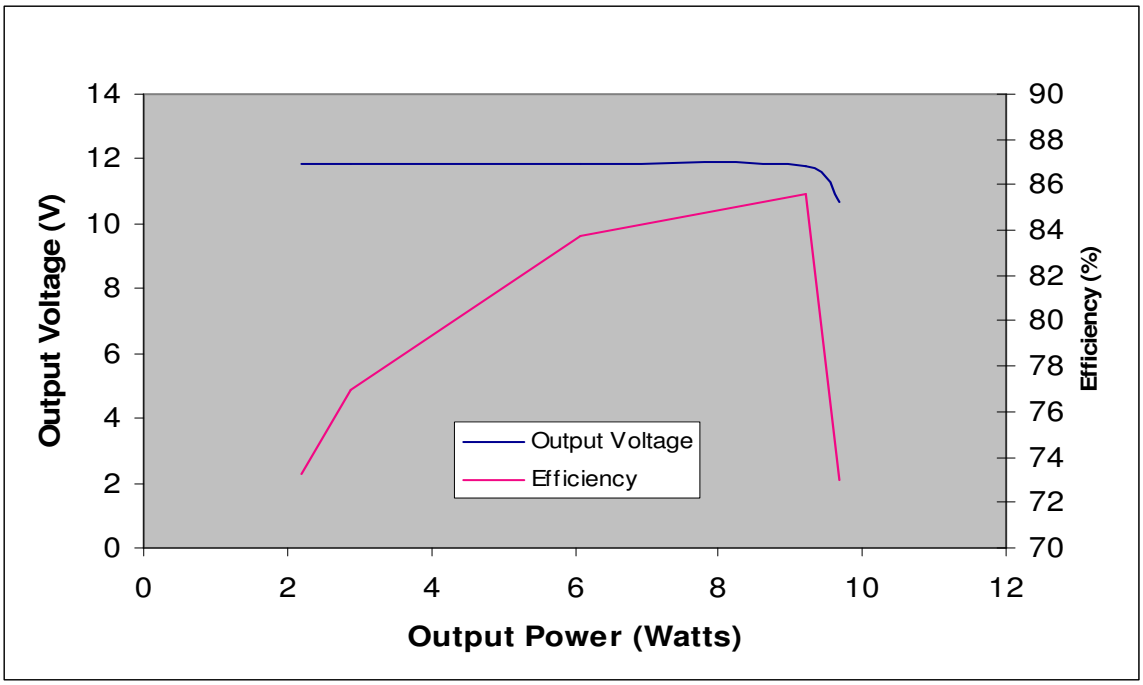

Figure 4.4 Output voltage and Efficiency of the converter at different load conditions for input voltage of 25V

CHAPTER 5: CONCLUSION

5.1 Summary

The ultimate goal of this research was to develop a method to manufacture thick magnetic cores with large number of laminations by automating the alternate metal electrodeposition process. A LabVIEW based robotic arm was successfully used as a wafer carrier between the alternate electroplating baths to develop laminated cores by controlling the current and time during the electrodeposition. For the same lamination manufacturing technique used, the automated electrodeposition allowed the fabrication of NiFe cores having ten times the number of laminations obtained in [6]. The inductors formed by hand winding the insulated magnet wire around the laminated cores were characterized for their inductance, Q factor and resistance. A low profile inductor having a core thickness of 600 microns was used to demonstrate a DC-DC buck converter. The 12V switching regulator had an efficiency of more than 76% for a load of 2-12 W at 2MHz for an input of 20V. The converter showed a decrease in the efficiency with increase in input voltage and load.

5.2 Future Suggestions

The inductors and power converter developed in the course of this research may be improved in terms of their inductance and power handling by employing some of the following suggestions.

The electroplating robot used in this research is not entirely a closed loop system. Many unmonitored parameters such as the composition of the electroplating baths lead to variation in the intrinsic properties of the electroplated material. pH control may lead to

better reproducibility of the process. Use of different magnetic alloys having more composition stability, higher permeability and resistivity than NiFe alloy can lead to improvement in the performance of the inductors. Use of ternary alloys like Ni-Fe-Mo and Co-Fe-X, where X is a non metallic element, give higher resistivity [30, 31]. A suitable sacrificial material with good selective etching over these alloys would give inductors with even lower core losses. Hand-wound wire may have lower resistance compared to micro fabricated windings but it adds to the bulkiness of the inductor. Laminated cores sandwiched between top and bottom coils printed on flexible substrates can be used to realize low profile inductors that can be stacked with the power management module. Fabrication of the inductors on top of prefabricated power management ICs is the final step towards development of ultra compact converters with higher performance.

APPENDIX A

A.1 Software for Current Control

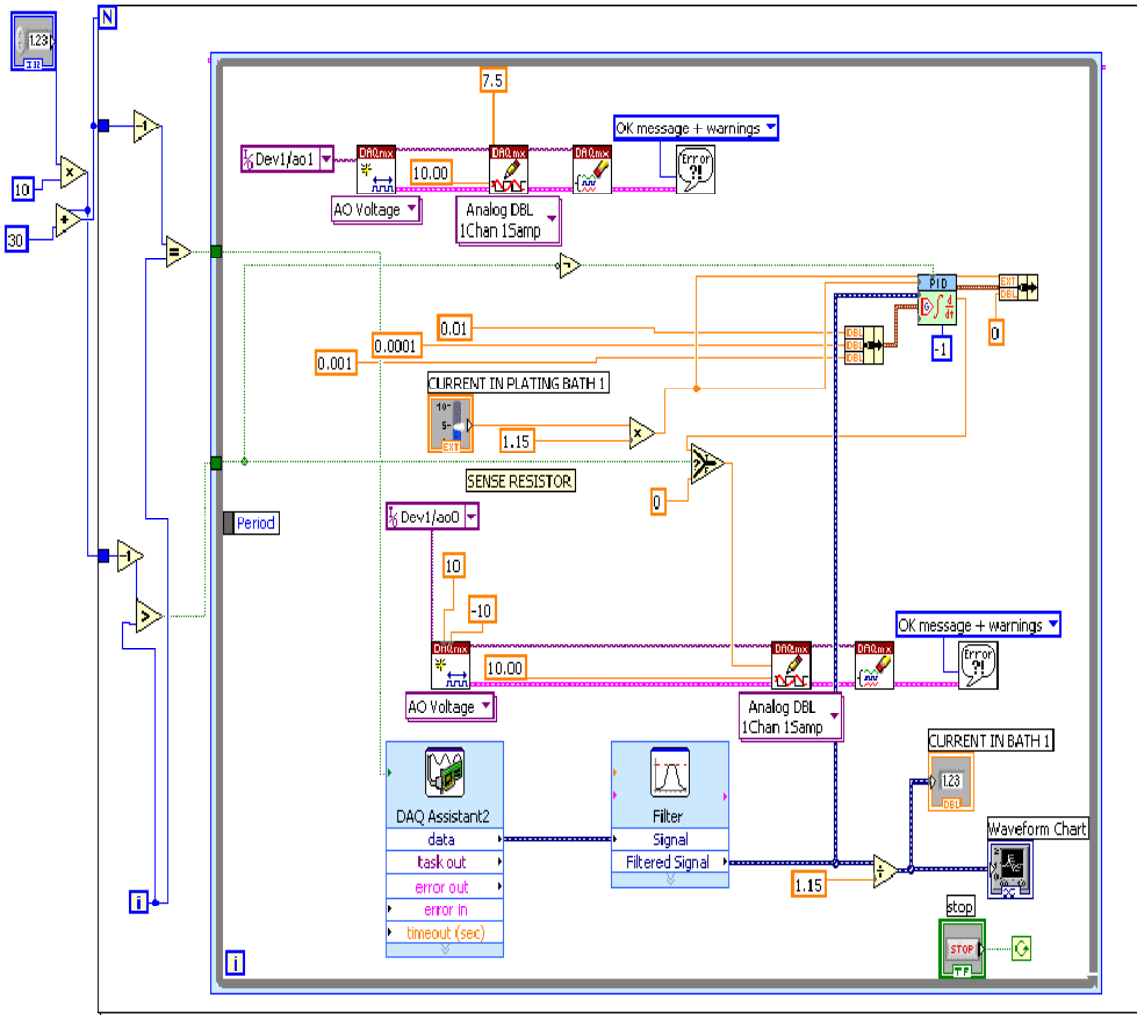

Figure A.1 Software block for current control

Figure A.1 shows the sub VI for precise current control. The outermost shell represents the FOR loop to operates for the input time N seconds. The inner shell is the synchronous time control loop operating at a frequency of 1KHz driven by an internal clock. The uppermost sequence inside the loop sets the gate voltage for T1 shown in figure 2.7. In order to ensure no overshoot in the current while loading the wafer in the bath and to precisely maintain the current in spite of change in plating resistance, a

proportional-integral-derivative (PID) controller is incorporated in the VI. The voltage measured across the sense resistor shown in figure 2.8 is filtered and input to the PID controller to correct the error between the measured value and the set value.

A.2 Software for dc motor control

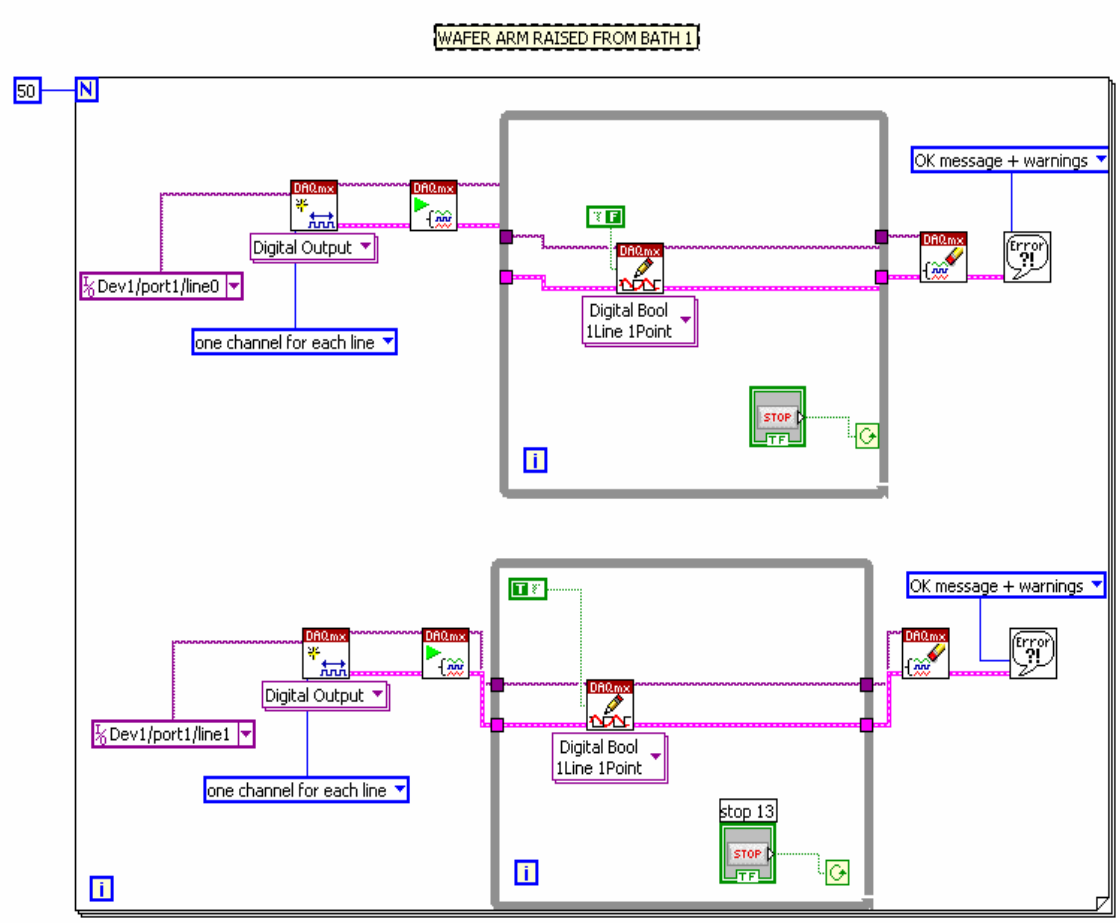

Figure A.2 Software block for dc motor control

As shown in table 2.1, a true signal is sent to one digital output port and false to the other to raise the arm out of the bath. In order to lower the arm, the signals are interchanged.

A.3 Software for position control

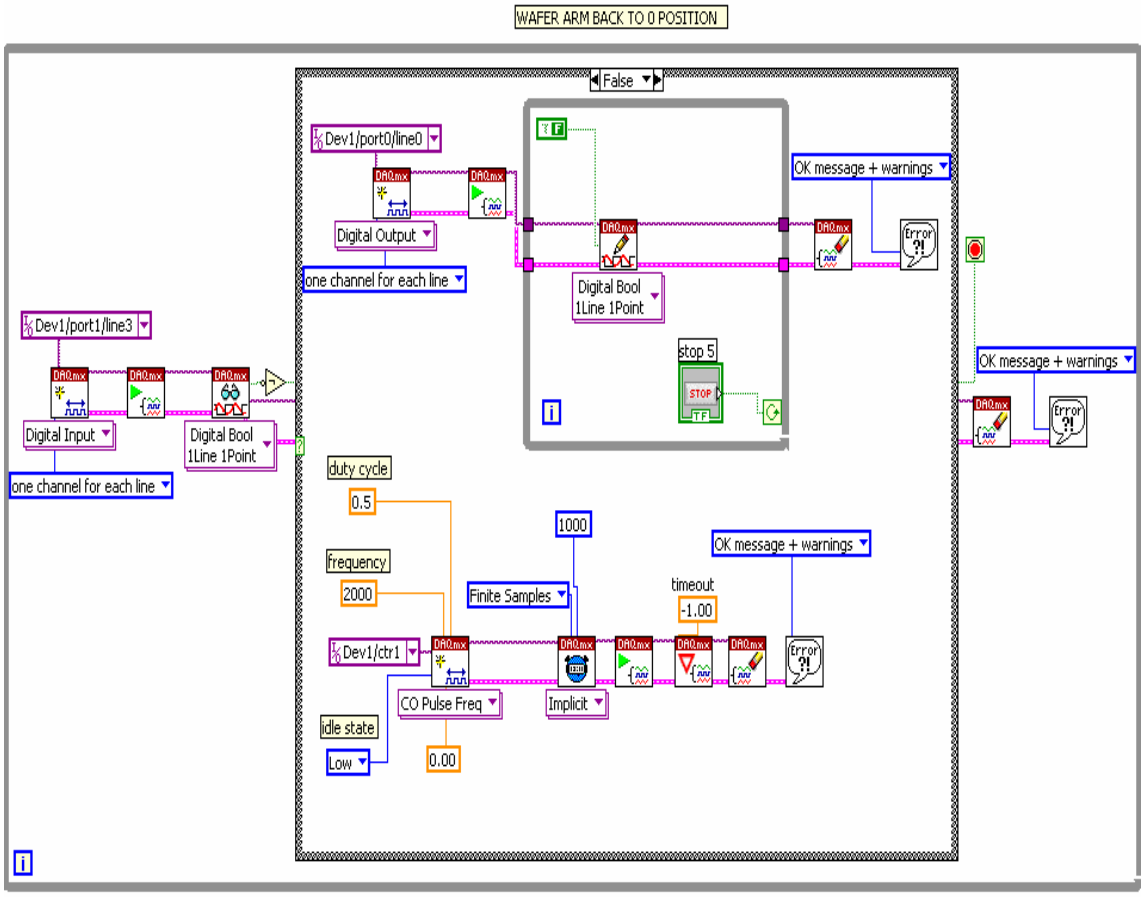

Figure A.3 Software block for position control

The optical sensor placed at the 0 position senses the arrival of the arm. The outermost WHILE loop shell operates while the arm is not in the zero position. The inner FALSE loop operates only when the input condition is false. If the arm is not in 0 position, the digital input port of the block receives a false signal and so the false loop sends a command signal to the motor driver to increment the motor step. When the arm reaches the home position, the digital input port receives a true signal and the process exits this block.

REFERENCES

1. *http://www.hills2.u-net.com/electron/induct.htm*l, Accessed: September, 2007

2. Brandon, E.J., et al., Fabrication and Characterization of Microinductors for Distributed Power Converters. IEEE TRANSACTIONS ON MAGNETICS, 2003. 39(4): p. 2049-2056.

3. Kaiser, C.J., The Inductor Handbook. CJ Publishing, April 1996.

4. Brunet, M., et al., Design study and fabrication for high power density microtransformers. Proceedings of IEEE Applied Power Electronics Conference, March 2001. 2: p. 1189-1195.

5. Park, J.-W., F. Cros, and M.G. Allen, Planar Spiral Inductors With Multilayer Micrometer-Scale Laminated Cores for Compact-Packaging Power Converter Applications. IEEE TRANSACTIONS ON MAGNETICS, 2004. 40(4): p. 2020-2022.

6. Park, J.-W. and M.G. Allen, Ultralow-Profile Micromachined Power Inductors With Highly Laminated Ni/Fe Cores: Application to Low-Megahertz DC-DC Converters. IEEE TRANSACTIONS ON MAGNETICS, 2003. 39(5): p. 3184-3186.

7. Park, J.-W., Core Lamination Technology For Micromachined Power Inductive Components. Ph.d Thesis, 2003.

8. Sullivan, C.R. and S.R. Sanders, Microfabrication process for high-frequency power-conversion transformers. 26th Anual Power Electronics Specialists Conference, June 1995: p. 658-664.

9. Kurata, H., et al., Study of thin film micro transformer with high operating frequency and coupling coefficient. IEEE TRANSACTIONS ON MAGNETICS, 1993. 29(6): p. 3204-3206.

10. Leith, S.D. and D.T. Schwartz, In-situ fabrication of sacrificial layers in electrodeposited NiFe microstructures. J. Micromech. Microeng., 1999. 9: p. 97-104.

11. Taylor, W.P., et al., A NiFeMo Electroplating Bath for Micromachined Structures. Electrochemical and Solid State Letters, 1999. 2(12): p. 624-626.

12. http://www.ni.com/pdf/products/us/20044546301101dlr.pdf., Accessed: October 2007.

13. http://www.techkits.com/SLA7062M.pdf., Accessed: October 2007.

14. http://focus.ti.com/lit/ds/symlink/tpic0108b.pdf., Accessed: September 2007.

15. http://www.ortodoxism.ro/datasheets/panasonic/CNZ1022.pdf., Accessed: July 2007.

16. Electroplating of nickel-iron alloys for uniformity of nickel/iron ratio using a low density plating current. United States Patent 4279707.

17. Lammeraner, J. and M. Stafl, Eddy Currents. Iliffe Books Ltd., 1966. Chapter 2.

18. Welsby, V.G., The theory and design of inductance coils. MacDonald and Co. Ltd, 1960.

19. *http://arxiv.org/pdf/cond-mat/0604442*.Accessed: October 2007.

20. Bertotti, G., General properties of power losses in soft ferromagnetic materials. IEEE TRANSACTIONS ON MAGNETICS, January 1988. 24: p. 621-630.

21. http://www.walkerldjscientific.com/Products/Product_Lines/Magnetic_Analysis/Hysteresisgraphs/HysteresisLosses.pdf., Accessed: August 2007.

22. Willard, M.A., T. Francavilla, and V.G. Harris, Core-loss analysis of an (Fe, Co, Ni)-based nanocrystalline soft magnetic alloy. Journal of Applied Physics, 2005. 97(10): p. 10-11.

23. Delage-Darces, M., et al., Prediction of Losses in Ferromagnetic Sheets: Dynamic and Magnetomechanical models. IEEE TRANSACTIONS ON MAGNETICS, September 200. 36(5): p. 3460-3462.

24. *http://nepp.nasa.gov/index_nasa.cfm/1003/*, Accessed: October 2007.

25. Mano, Y., et al., Planar Inductor With Ferrite Layers For DC-DC Converter. Transducers' 05, The 13th International Conference on Solid-State Sensors, Actuators and Microsystems, June 2005: p. 891-894.

26. Sasada, I., et al., Planar Inductors Using NiZn Ferrite Thin Plates and the application to high frequency DC-DC converters. IEEE TRANSACTIONS ON MAGNETICS, November 1993. 29(6): p. 3231-3233.

27. Schelle, D. and J. Castorena, Buck-Converter Design Demystified. Power Electronics Technology, June 2006: p. 46-53.

28. Mohan, N., T.M. Undeland, and W.P. Robbins, Power Electronics: Converters, Applications, and Design. John Wiley and Sons, Inc.

29. Datasheet-LT3481 Linear Technology.

30. Liakopoulos, T.M., R.W. Filas, and A. Lotfi, Post-CMOS integrated planar inductors for monolithic power management chips. Proc. Electrochemical Society: Magnetic Materials, Processes and Devices VI, 2000. 29: p. 580-591.

31. Ha, N.D., et al., High frequency permeability of soft magnetic CoFeAlO films with high resistivity. Journal of Magnetism and Magnetic Materials, April 2005. 290-291(Part 2): p. 1571-1575.